ESTIMATION OF THE VERTICAL WAVELENGTH OF ATMOSPHERIC GRAVITY WAVES FROM AIRGLOW IMAGERY

BY

UDAY KANWAR

THESIS

Submitted in partial fulfillment of the requirements
for the degree of Master of Science in Electrical and Computer Engineering
in the Graduate College of the
University of Illinois at Urbana-Champaign, 2011

Urbana, Illinois

Adviser:

Associate Professor Jonathan Makela

ABSTRACT

In the summer of 2010, two imagers were installed in New Mexico with the objective of making stereoscopic observations of atmospheric gravity waves (AGWs). As AGWs propagate vertically, they spatially perturb the airglow emission layers in all three dimensions. Estimates of the vertical wavelength, horizontal wavelength, and the intrinsic frequency are needed to characterize an AGW and quantify its effects on upper atmospheric dynamics. The dispersion relation describes the relationship between vertical and horizontal wavelengths as a function of the intrinsic frequency. Thus, any two of the three aforementioned parameters can be used to determine the third. Mesospheric winds are hard to measure and consequently the intrinsic frequency is difficult to estimate. However, the horizontal wavelength can be directly measured from airglow imagery once the three-dimensional imager field of view is projected onto the two-dimensional image plane. This thesis presents a method to estimate the vertical wavelength using an airglow perturbation model proposed by *Anderson et al.* [2009]. The model is subsequently validated using the observations from ground-based imagers installed in New Mexico.

The perturbed airglow is modeled as a quasi-monochromatic wave and thus, it can be characterized using only a few parameters, one of which is the vertical wavelength, λ_z. Because λ_z is embedded in both the phase and the magnitude of this model, two values of λ_z are estimated by applying two different parameter estimation techniques on the phase and magnitude. The estimation of λ_z from the phase of the model entails solving an overdetermined system of linear equations by

minimizing the sum of the squared residuals. This estimate is then compared to that obtained by iteratively finding the best approximation to the roots of a function, representing the magnitude of the perturbation model. These two techniques are applied on three nights in 2010, and the estimates for λ_z match to within a few kilometers. Thus, the perturbation model is validated using real data.

To my parents, Aruna and Neeraj Kanwar, for their unconditional love and support.

To S. K. Sharma, my role model, inspiration and life mentor, for sparking my curiosity in engineering and instilling in me values of truth, integrity and discipline.

ACKNOWLEDGMENTS

Thanks to my adviser Professor Jonathan Makela whose inspirational instruction and guidance have been monumental. I would like to acknowledge Professor Erhan Kudeki for investing his faith in my abilities and giving me the confidence to excel. I am grateful to Dr. Scott Anderson for his patience and help at every stage. I would like to thank the Office of Naval Research (ONR) for supporting my studies through grant N00014-09-1-0439. I am also grateful to my colleagues in the Remote Sensing and Space Sciences group: Narayan Chapagain, Timothy Duly, Daniel Fisher, Thomas Gehrels, Levent Gezer, Brian Harding, Yiyi Huang, James Law, Tony Mangognia, Serge Minin, Pablo Reyes and Fabio Vargas. Finally, I would like to thank my friends and family outside of lab who completed the ecosystem that made this thesis possible: Trishla Bhargava, Sudeep Gowrishankar, Ananya Kanwar, Esha Kanwar, Pankaj Kanwar, Sukhda Kanwar, Sushil Kanwar, Pavithra Raju and Rithwick Varier.

TABLE OF CONTENTS

Page

LIST OF TABLES vii

LIST OF FIGURES viii

CHAPTER 1 MOTIVATION 1

CHAPTER 2 INTRODUCTION 4
2.1 Atmospheric Gravity Waves 4
2.2 Airglow Emission 9
2.3 Modulation of the Airglow by Atmospheric Gravity Waves 12
2.4 Historical Review of the Estimation of λ_z 15
2.5 Conclusion 18

CHAPTER 3 PARAMETER ESTIMATION 19
3.1 Airglow Perturbation Model 20
3.2 Gabor Filtering 25
3.3 Parameter Estimation 29
3.3.1 Phase Analysis 30
3.3.2 Magnitude Analysis 32
3.4 Conclusion 35

CHAPTER 4 DATA ANALYSIS 37
4.1 Instrumentation 37
4.2 Preprocessing 42
4.3 Results 44
4.3.1 15 May 2010 44
4.3.2 16 May 2010 52
4.3.3 2 September 2010 55
4.4 Summary 59

CHAPTER 5 CONCLUSIONS 60

REFERENCES 62

LIST OF TABLES

Table Page

2.1 The wavelengths of the commonly observed airglow emissions in the mesosphere 12

4.1 Timestamps of the images used for phase analysis, 15 May 2010 . . . 49
4.2 Timestamps of the images used for phase analysis, 16 May 2010 . . . 54
4.3 Timestamps of the images used for phase analysis, 2 September 2010 59
4.4 Summary of the results 59

LIST OF FIGURES

Figure Page

2.1 Wave vectors and wave fronts for an upward propagating wave where β is the angle between the wave vector and the horizontal. 7

2.2 Sodar images of gravity waves in the planetary boundary layer plotted on a log-scale (after *Zamora* [1983]). 8

2.3 (a) Airglow emission spectra obtained by Bradfoot using a spectrophotometer (after *Bradfoot and Kendall* [1968]). (b) Airglow emission spectra obtain using a charged coupled device (CCD) imaging spectrograph (after *Sharp* [1986]). 1 Å = 0.1 nm. In both images of the absorption spectra, there is a sharp peak at 6300 Å related to a chemiluminescent reaction associated with atomic oxygen. 10

2.4 The transition of the excited atomic oxygen species to more stable states results in the emission of a photon. Shown are the transitions $^1S \rightarrow {}^1D$ (557.7 nm) and $^1D \rightarrow {}^3P$ (630.0 nm). 11

2.5 The volume emission rates of the most commonly imaged airglow layers in the mesosphere. The emissions are not localized at a particular height and are dependent on the neutral density and temperature of the mesosphere at those heights (after *Liu and Swenson* [2003]). . . . 13

2.6 The vertical profile of a modeled hydroxyl airglow emission. The thin solid lines represent a time-sequential series, the thick solid curve represents the average emission profile, the thin dashed curves represent the time differenced perturbation profiles, while the thick dashed curve shows their envelope (after *Swenson et al.* [2005]; *Liu and Swenson* [2003]). 15

2.7 One of the first infrared images of the airglow perturbed by atmospheric gravity waves (after *Peterson and Kieffaber* [1973]). 16

3.1 Four images showing examples of gravity wave structure recorded in the OI(557.7 nm) and near-infrared OH emissions during the campaign: (a, b) extensive bands; (c) example of transient ripples and (d) a complex mixture of band and ripple waves. Note that the oval silhouette at the bottom of each image is the Instituto Nacional de Pesquisas Espaciais satellite tracking antenna, while the dark patches at low elevations in (b) and (c) are clouds (after *Taylor et al.* [1997]). 20

3.2 The observation geometry of the airglow layer and the imager. Here, the imager co-ordinates are (x_0, y_0, z_0) and the line-of-sight vector is (x', y', z') (after *Anderson et al.* [2009]). 22
3.3 (a), (b) Optical images from Socorro and the National Solar Observatory in New Mexico. (c), (d) Geometric transformation of (a) and (b) to a common unified co-ordinate system. 25
3.4 The Fourier transform of the model in Equation 3.6 will be a two-dimensional spatial Gaussian function that is centered at the spatial frequencies (k_x, k_y) along with its complex conjugate term centered at $(-k_x, -k_y)$. 26
3.5 The spectral response of the Gabor filter is plotted when q_x and q_y are equal (a), $q_x > q_y$ (b) and $q_x < q_y$ (c). 27
3.6 Equation 3.8 illustrated. The magnitude of the filtered image resembles a Gaussian indicating that the Gabor filter is matched to the AGW characteristics. 28
3.7 A filter bank obtained after filtering airglow images for a whole night with different values of T and θ. The parameters for the Gabor filter, T and θ, corresponding to the region where the intensity is maximum is chosen, indicated here by a white circle. 29
3.8 The Newton-Raphson algorithm for a function $f(x)$ finds the zero of the function by iterating through a set of points that eventually converge to the root. 33

4.1 The imagers at Socorro and NSO have three components - the objective lens, the filter wheel and the CCD sensor array. The objective lens, at the top, with a field of view of 180°, screws on to the filter wheel whose bottom side is friction fit with a black cylindrical metallic tube that is aligned over another set of focussing optics and the CCD. 39
4.2 (a) Greenline emission at 557.7 nm acquired by the NSO imager on 15 May 2010 at 06:33:15 UT. (b) Image of the background that is closest taken immediately after. (c) Average image of the night that is used to normalize the background subtracted raw image to correct for differing sensitivities of the two imagers. (d) Result of this process. 43
4.3 The raw airglow image of the perturbed greenline emission layer taken from NSO (a), and Socorro (b), at 06:33:15 UT. 44
4.4 A series of projected images of the greenline emission layer taken from the two imagers, showing the propagation of the wavefronts in the northwest direction. 45
4.5 The projected images of the perturbed greenline layer, taken from NSO, are Gabor filtered with T, ranging from 20 to 50 km, and θ, ranging from 0 to 180°. The magnitude of the output at the center, (0,0), is plotted. A high magnitude will indicate a well matched filter. 46

4.6 The magnitude of the filtered image where the filter parameters T and θ are matched to the spatial frequencies of the observed AGW. $T = 46$ km and $\theta = 128°$. 47
4.7 The five points chosen have the co-ordinates (-50, -14), (29, -36), (0, -40), (32, -15) and (14, -48) on both the imagers giving a total of ten measurements of $|G(x, y)|$. The data, $|G(x, y)|$, is plotted over the model, Z_n, and it is seen that the model fits the data well with $\lambda_z = 64.6$ km. 48
4.8 A local minimum is found by holding four of five points constant and finding the fifth point that minimizes the function. Then, the first three and the fifth point are held constant to find a new fourth point that minimizes the function. This process continues till five points are found that satisfy all the constraints. The figure shows how a single point, (64,-17), is improved to (69,-13) as the function is lower there. 49
4.9 As the phase is in its principal phase it must be unwrapped before solving the system of equations. The phase of the greenline emission is plotted for three time instances . A factor of 2π is added to $\angle G(x, y)$ of the third time instance as the wave has propagated a full phase. . . 50
4.10 $\angle G(x, y)$ for all the three layers against time, in minutes, that is differenced to the time of the first observation. It can be inferred that along every emission layer there exists a constant slope implying a constant horizontal phase velocity of the wave. $\lambda_z = 64.0$ km. . . . 51
4.11 The projected airglow images acquired from NSO and Socorro at 07:54:16 UT on 16 May 2010. 52
4.12 The parameters of the Gabor filter, T and θ, are determined from an exhaustive search with T ranging from 12.6 to 31.4 km and θ from 0° to 180°. $T = 20$ km and $\theta = 118°$. 53
4.13 The five points chosen for the magnitude analysis are (10,-45), (17,-93), (-8,-67), (50,-44) and (-19,-2). For this set of points the model converges to the data, with $\lambda_z = 25.7$ km. 53
4.14 $\angle G(x, y)$ for all the three layers against time, in minutes, that is differenced to the time of the first observation. It can be inferred that along every emission layer there exists a constant slope implying a constant horizontal phase velocity of the wave. $\lambda_z = 25.7$ km. . . . 54
4.15 The projected airglow images acquired from NSO and Socorro at 05:13:02 UT on 2 September 2010. The five red points are used towards the magnitude analysis 56
4.16 The parameters of the Gabor are determined, $T = 36.5$ km and $\theta = 55.2°$. The figure plots the magnitude of the filtered image. The black crosses denote the five points - (31,-3), (41,-18), (34,38), (50,-22) and (31,18) - used towards the magnitude analysis. 57
4.17 The model, Z_n, and the ten data points, $|G(x, y)|$, are plotted and there is excellent match between the two with $\lambda_z = 41.8$ km. 57

4.18 $\angle G(x, y)$ for all the three layers against time, in minutes, that is differenced to the time of the first observation at 5:03:02 UT on 2 September 2010. It can be inferred that along every emission layer there exists a constant slope implying a constant horizontal phase velocity of the wave. $\lambda_z = 41.5$ km. 58

CHAPTER 1

MOTIVATION

Over the past decade or so climate change has been acknowledged as a significant challenge facing our society. The three warmest years on record have all occurred since 1998 and 19 of the warmest 20 since 1980 [*Pearce*, 2006]. Climate change has manifested in a variety of ways, from the melting of the Arctic ice and permafrost to lethal hurricanes and tsunamis. Thus, understanding what affects global patterns in winds, heat transfer, radiation and humidity is imperative. The effects of large- and small-scale disturbances on the transport of ozone and ozone-destroying chemicals must be incorporated into mathematical models, like the middle atmosphere general circulation models (GCMs), that are used to estimate and predict climate change. Atmospheric gravity waves (AGWs) are one such disturbance that is responsible for distributing energy and momentum from the troposphere to the upper atmosphere.

The term *atmospheric gravity waves* was used first by Colin Hines [*Hines*, 1965] to describe wave motion that can propagate through fluids whose density increases with depth. The atmosphere is one such fluid that is stratified by the force of gravity. The waves may propagate vertically or horizontally or appear stationary; they may reflect or seem to break apart into smaller waves that eventually dissipate. Spectrally they are diverse as well, and at times there exist high-frequency waves superimposed over low frequency waves; some may have large amplitudes while others are barely discernible. Gravity waves are not visible to the naked eye, but

their effects on the atmosphere can be measured and observed using several different techniques. Between 80 and 120 km in the upper atmosphere over middle and low latitudes there exist profiles of photochemical luminescence caused by reactions of various atmospheric gases; this phenomenon is known as *airglow*. As gravity waves propagate vertically, they spatially perturb the airglow emission layers in all three dimensions. In this thesis, we show how airglow perturbation models along with measurements from different airglow layers can be used to estimate the parameters of AGWs and quantify their effects.

The dispersion relation for an AGW describes the relationship between its horizontal and vertical frequencies as a function of the intrinsic frequency. The term *intrinsic* implies a property of the wave in the reference frame of the background mesospheric wind. From measurements of any two of the three aforementioned parameters, the third can be easily determined. The horizontal wavelength can be directly measured from airglow imagery once the three-dimensional imager field of view is projected onto the two-dimensional image plane. The mesospheric wind and, thus the intrinsic frequency, is hard to measure. Therefore, the problem of quantifying the energy transported by AGWs is reduced to the determination of the vertical wavelength. Tomography has been extensively employed as an approach to study the vertical structure of the ionosphere. In the 1980s radio tomography was used to reconstruct the total electron content (TEC) at different heights [*Austen et al.*, 1988] and to study ionospheric phenomena like equatorial bubbles and the ionospheric trough [*Austen et al.*, 1986]. With rapid improvements in optics and electronics, more sophisticated techniques in tomography were employed, like the three-dimensional reconstruction of an auroral arc in Norway [*Frey et al.*, 2001] that adapted an inversion algorithm to reduce the error in the estimates. In general, the results of tomographic inversions strongly depend on the quality of the observational geometry, motivating the study of ground-based measurement techniques that can

reliably estimate the vertical characteristics.

In *Anderson et al.* [2009] an airglow perturbation model for data collected from ground-based imagers is developed on the premise that the perturbation is wavelike. Under this assumption, the problem is simplified, as only a few parameters are needed to completely represent the perturbation, and thus the complexity of the estimation process is reduced as compared to full-blown tomography. Moreover, it can be argued that given observations from two imagers this technique is more robust than tomographic inversion for which, as shown in *Nygren et al.* [2000], a chain of more than two imagers must be established for reasonable results. The goal of this thesis is to validate this perturbation model.

Chapter 2 examines the relationship between AGWs and airglow emissions along with a brief overview of previous work in the area. The relationship is quantified as Chapter 3 derives the model of the airglow perturbation as observed by a ground-based imaging instrument. Chapter 4 then describes the instrumentation deployed in New Mexico and introduces two techniques to estimate the vertical wavelength. The unknown vertical wavelength is embedded in the phase and magnitude of the model; the two are solved independently to arrive at estimates for the vertical wavelength. The observed airglow data are then used to validate these techniques. In Chapter 5, a conclusion of this work is presented along with a discussion on the results.

CHAPTER 2

INTRODUCTION

This chapter describes some introductory concepts to facilitate the understanding of advanced topics discussed later in the thesis.

2.1 Atmospheric Gravity Waves

The atmosphere is a continuous fluid with a density that increases with depth - a stably stratified fluid. One of the properties of a stably stratified fluid is its ability to support and propagate wave motions. Within the atmosphere, the driving mechanism behind these waves is the buoyant force that works to restore a displaced air parcel from equilibrium. If an air parcel is displaced vertically by δz such that the process is adiabatic, i.e., there is no net transfer of heat across the surface of the air parcel, its motion can be expressed as follows [*Nappo*, 2002]:

$$\frac{d^2\left(\delta z\right)}{dt^2} = -\frac{g}{\rho_0}\frac{\partial \rho_0}{\partial z}\delta z. \tag{2.1}$$

This second order differential equation describes a simple harmonic motion of an air parcel in the vertical direction. The negative sign implies that the restoring force acts in the opposite direction to the displacement. The term ρ_0 is the density of the

environment of the air parcel. The solution of Equation 2.1 is expressed as

$$\delta z(t) = Ae^{jNt} + Be^{-jNt}, \tag{2.2}$$

where $N = \sqrt{\frac{g}{\rho_0}\frac{\partial \rho_0}{\partial z}}$. In a stably stratified fluid $\frac{\partial \rho_0}{\partial z} > 0$, N is real and thus motion is possible. When $\frac{\partial \rho_0}{\partial z} < 0$ and N is imaginary, Equation 2.2 represents an instability stemming from the unbounded growth of the amplitude known as a convective instability. This frequency, N, for vertically propagating gravity waves is known as the Brunt-Väisälä frequency.

The Taylor-Goldstein equation [*Taylor*, 1931; *Goldstein*, 1931] forms the basis for studying wave phenomena in the upper atmosphere. The equation is derived by simultaneously solving the two-dimensional Euler equations of motion, which describe the conservation of momentum, mass and thermal energy of an irrotational and frictionless atmosphere. Perturbations in the atmosphere like turbulence, density currents and thermal plumes contribute to the non-linear nature of the observed wave characteristics like momentum and energy. In order to simplify the analysis without the loss of accuracy, linear theory is applied according to

$$q(x, z, t) = q_0(z) + q_1(x, z, t), \tag{2.3}$$

where $q_0(z)$ is a slowly varying, horizontally uniform background value and $q_1(x, z, t)$ is a perturbation value that is assumed to be much smaller than the background value. Equation 2.3 also implies that the perturbations do not affect the background state, whereas in reality interaction between the two results in complex wave structures with time-varying amplitudes at several frequencies [*Hauf et al.*, 1996; *Einaudi and Finnigan*, 1981]. *Dornbrack* [1998] tested the validity of these assumptions by comparing results of a linear wave model with those from a non-

linear time-dependent numerical model, and it was concluded that for important wave parameters the linear model was accurate. The Taylor-Goldstein equation is further simplified by neglecting the effects of the rotation of the earth and assuming zero background wind speed, after which it is expressed as

$$\frac{d^2\hat{w}}{dz^2} + \left[\frac{k^2N^2}{\omega^2} - k^2\right]\hat{w} = 0. \tag{2.4}$$

Equation 2.4 is the wave equation for linear gravity waves represented by $\hat{w}(z)$, where $k = \sqrt{k_x^2 + k_y^2}$ is the horizontal wavenumber and ω the angular frequency of the wave. Its general solution is

$$\hat{w}(z) = Ae^{jk_z z} + Be^{-jk_z z}, \tag{2.5}$$

where the vertical wavenumber, k_z, can be expressed in terms of the angular frequency, ω, giving the dispersion relation

$$k_z^2 = k^2\left[\frac{N^2}{\omega^2} - 1\right]. \tag{2.6}$$

Equation 2.6 expresses the relationship between the wave structure and the physical characteristics of the atmosphere. Rearranging Equation 2.6, we get

$$\omega = \frac{kN}{(k^2 + k_z^2)^{1/2}} = N\cos\beta, \tag{2.7}$$

where β is the angle between the wave vector and the horizontal as shown in Figure 2.1. Equation 2.7 implies that the maximum possible angular frequency of a wave is the Brunt-Väisälä frequency, N. When β is zero, the fluid particles oscillate vertically at a frequency, N, which is the resonant frequency of the fluid and thus any excitation beyond this would not be supported by the fluid buoyancy. Using

Equation 2.7, the vertical group velocity, $w_g = \frac{\partial \omega}{\partial k_z}$, is determined and expressed as

$$w_g = -\frac{k k_z N}{(k^2 + k_z^2)^{3/2}} = -c_z \sin^2 \beta, \tag{2.8}$$

where c_z is the vertical phase velocity. This equation shows that the group and phase velocities will always be in the opposite direction as $sin^2\beta$ is always positive; that is, if wave fronts are propagating downwards, then the wave energy propagates upwards.

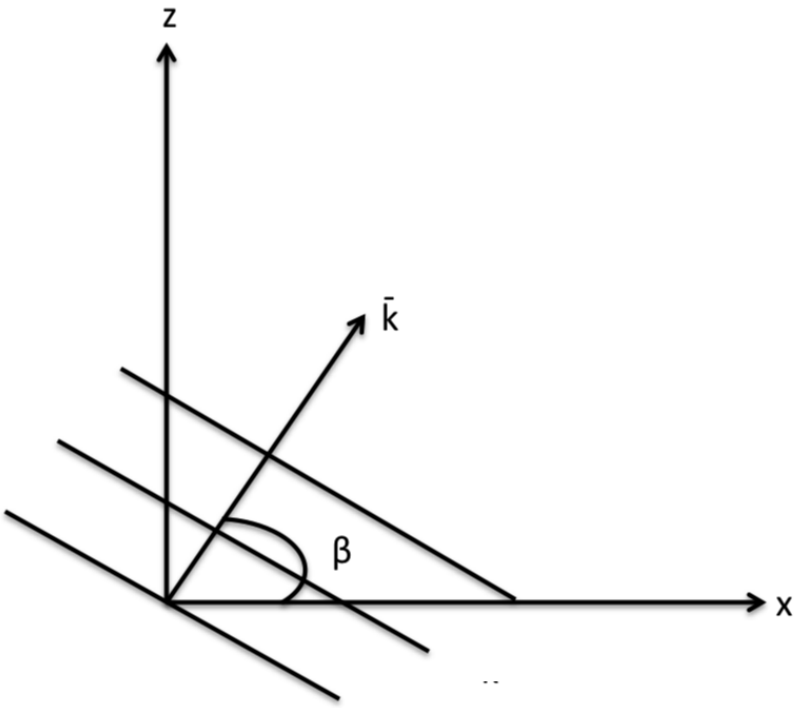

Figure 2.1 Wave vectors and wave fronts for an upward propagating wave where β is the angle between the wave vector and the horizontal.

The vertical energy flux of a gravity wave is derived from the mean energy density [*Gossard and Hooke*, 1975] expressed as

$$J = \frac{1}{2}\rho_0 \left[\bar{V}^2 + N^2 \bar{\zeta}^2\right], \tag{2.9}$$

where ρ_0 is the background atmospheric density, $\bar{V}^2$ the wave kinetic energy and $N^2\bar{\zeta}^2$ the potential energy due to vertical displacements, ζ. By taking the product of Equations 2.8 and 2.9, the vertical energy flux is given as [*Fritts and Vincent*, 1987]

$$F_\epsilon = -\frac{\rho_0 \omega^2 g^2}{k_z^2 N^2} \left\langle \left(\frac{\rho_1}{\rho_0} \right)^2 \right\rangle, \tag{2.10}$$

where g is the acceleration due to gravity, and $\frac{\rho_1}{\rho_0}$ is the relative density perturbations in the atmosphere. As gravity waves propagate vertically, they transport energy and momentum from the troposphere to the upper atmosphere and play a crucial role in determining its large-scale dynamics.

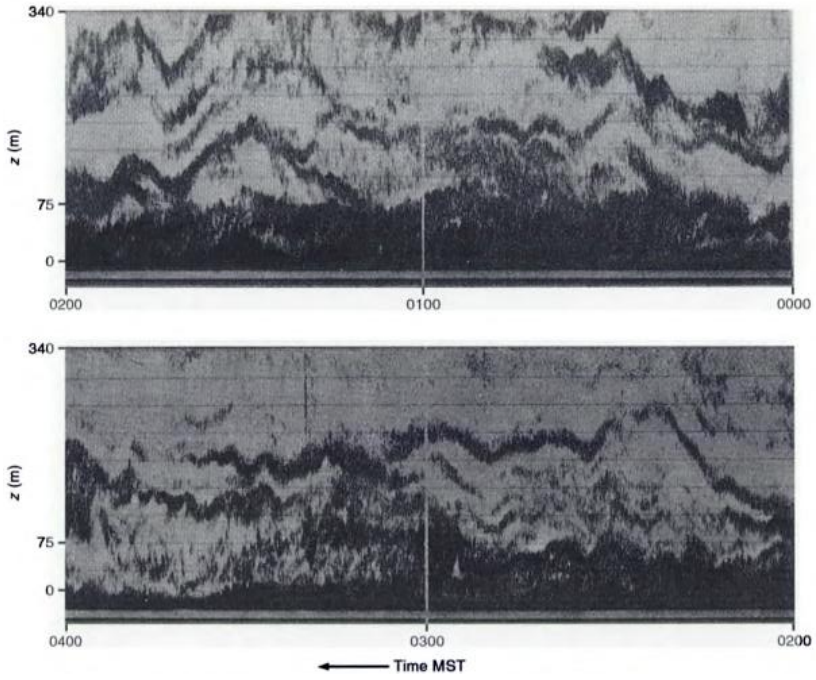

Figure 2.2 Sodar images of gravity waves in the planetary boundary layer plotted on a log-scale (after *Zamora* [1983]).

Figure 2.2 shows images [*Zamora*, 1983] of AGWs as probed by a sodar - an instrument that measures the scattering of sound waves by atmospheric turbulence. This was part of an exercise to characterize the atmosphere by determining the ratio of the acting inertial and viscous forces, known as the Reynolds number. Fig-

ure 2.2 clearly shows the wavelike structure in the vertical dimension illustrating the complexity of the problem at hand. AGWs have a wide ranging spectrum of frequencies and amplitudes, and propagate in all three dimensions. The following section introduces the phenomenon of airglow as a tool to study and parameterize AGWs.

2.2 Airglow Emission

In the upper atmosphere there is continual emission of light due to photochemical reactions of neutral and ionized constituents. Atmospheric species, excited by the ultraviolet solar radiation, drop to a lower level of excitation by either spontaneous emission of a photon or by losing energy through a collision. This phenomenon of optical emission is termed *airglow*.

The intensity of the airglow is measured in terms of the volume emission rate, which is the number of photons emitted per unit volume of the line-of-sight column. The reacting species, chemical kinetics and intensity are all dependent on the temperature and molecular density profile of the mesosphere and thus are not localized at a single altitude. Diffusion of molecules across these heights may catalyze several kinds of photochemical reactions that are also affected by the seasonal variations of mesospheric temperatures as studied by *Solomon and Garcia* [1987]; *Solomon et al.* [1984]. There are three major classes of visible airglow emissions in the mesopause layer: (1) the vibrational-rotational bands of OH, (2) the atomic and molecular emissions of oxygen, and (3) the emissions of metallic atoms such as sodium, calcium, potassium, and magnesium.

Discovered first by *Meinel* [1950], the vibrational bands of OH range from 500 nm to 2700 nm with the majority of photons being produced in the infrared region of the visible spectrum. The near infrared portion of the visible spectrum as measured

by a spectrophotometer is illustrated in Figure 2.3 [*Bradfoot and Kendall*, 1968], and a charged coupled device (CCD) imaging spectrograph in 2.3 [*Sharp*, 1986]. By studying the features of the peaks, the rotational temperatures are estimated and reaction mechanisms are proposed [*Sharp*, 1986]. The prominent peak in the absorption spectra is that of atomic oxygen at 630 nm. Thus, airglow emission peaks are observed at wavelengths which are dependent on the chemistry of the reacting species.

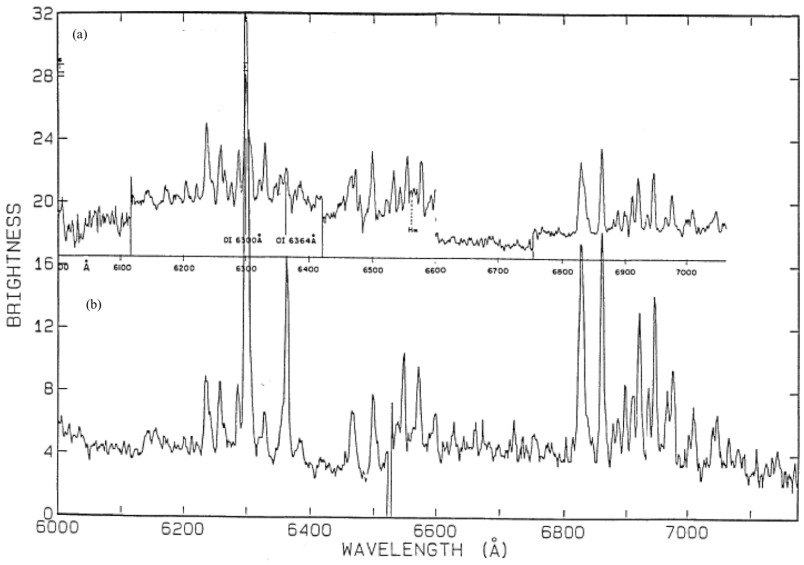

Figure 2.3 (a) Airglow emission spectra obtained by Bradfoot using a spectrophotometer (after *Bradfoot and Kendall* [1968]). (b) Airglow emission spectra obtain using a charged coupled device (CCD) imaging spectrograph (after *Sharp* [1986]). 1 Å = 0.1 nm. In both images of the absorption spectra, there is a sharp peak at 6300 Å related to a chemiluminescent reaction associated with atomic oxygen.

The two most important emission lines related to the atomic and molecular emission of oxygen occur at 557.7 nm and 860-870 nm. These spectral bands are strongest in terms of the volume emission rate of the photons emitted and are thus observed with ease by optical instruments. Figure 2.4 illustrates the state transitions $^1S \rightarrow {}^1D$ and $^1D \rightarrow {}^3P$ of excited species of atomic oxygen that are accompanied

by photons emitted at 557.7 nm and 630.0 nm, respectively. The photochemistry is governed by the Chapman and Barth mechanisms and is well reviewed in the literature [*McDade et al.*, 1986; *Torr et al.*, 1985; *Bates*, 1978, 1981].

The primary source of metallic species in the mesosphere has been attributed to meteoric ablation. The evidence includes strong correlation between relative abundances of metallic ions, observed in the lower thermosphere, to meteor showers [*Grebowsky and Aikin*, 2002; *Kopp*, 1997]. Lidar observations have also revealed the phenomenon of sudden neutral metal layers that are thin, concentrated layers of Na, K, Fe and Ca occurring at altitudes between 90 and 110 km. The average width of these sporadic layers is only about 2 km, and their peak concentration can be as much as 40 times the peak of the background metal layer [*Kane et al.*, 1993].

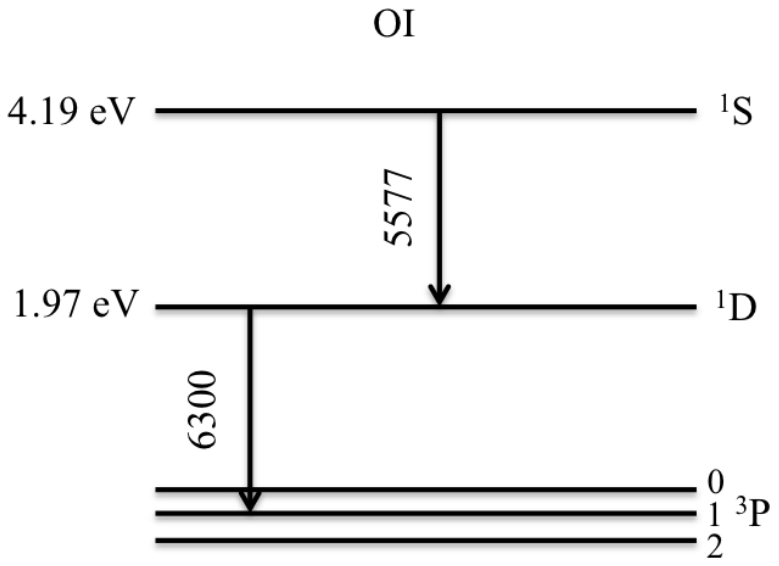

Figure 2.4 The transition of the excited atomic oxygen species to more stable states results in the emission of a photon. Shown are the transitions $^1S \rightarrow {}^1D$ (557.7 nm) and $^1D \rightarrow {}^3P$ (630.0 nm).

Thus, by using optical filters to isolate specific emissions along with CCD imagers with exposure times of a few minutes, we can image a particular airglow emission.

The four most commonly observed airglow emissions in the mesosphere are those resulting from transitions between different states of hydroxyl (OH), molecular oxygen (O_2), atomic oxygen (OI) and sodium (Na). Table 2.1 summarizes the important wavelengths in the spectra of the four commonly observed airglow emissions. The following section describes how the airglow is modulated by gravity waves.

Table 2.1 The wavelengths of the commonly observed airglow emissions in the mesosphere

	Emission Wavelength (nm)
OH	780-2000
O_2	860-870
OI	557.7
Na	589.9

2.3 Modulation of the Airglow by Atmospheric Gravity Waves

The airglow emission chemistry is dependent on the temperature and density of the reacting species. The seasonality in mesospheric winds and temperatures can alter the local atmosphere and, thus, the emission characteristics. It was reported by *Cogger et al.* [1981] that the combination of the diffusion of atomic oxygen from the lower thermosphere with a weak meridional circulation cell led to a buildup of O in the mesopause region. This change manifested with an increase in the green-line (557.7 nm) intensity. A similar study was conducted by *Texier et al.* [1987] to correlate modeled seasonal variations in the mesosphere with the variations in intensity of the OH emission. Apart from seasonal variations, there are several dynamical processes in the atmosphere, like thermal tides and planetary waves, that

transport momentum and alter the mesospheric structure. Other sources of mesospheric variability have been reviewed in *Solomon and Garcia* [1987]. Atmospheric gravity waves are another major source of density and temperature variations in the mesosphere.

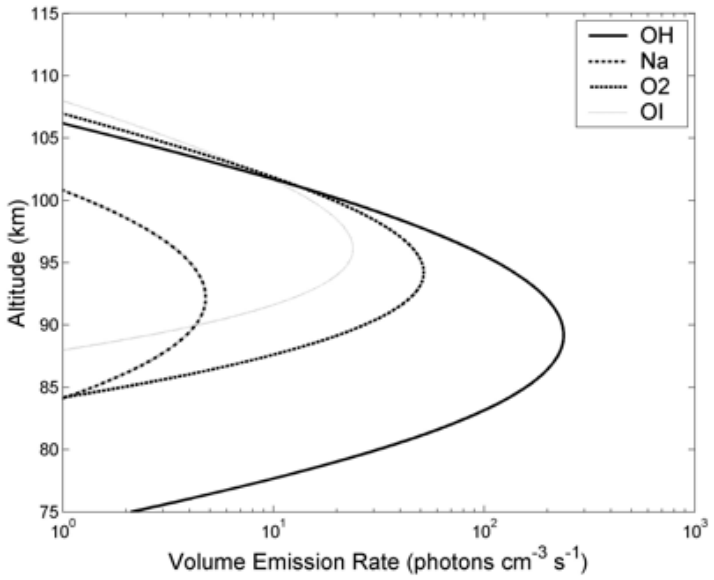

Figure 2.5 The volume emission rates of the most commonly imaged airglow layers in the mesosphere. The emissions are not localized at a particular height and are dependent on the neutral density and temperature of the mesosphere at those heights (after *Liu and Swenson* [2003]).

As AGWs propagate vertically they transport energy and momentum, thereby altering large-scale dynamics of the mesosphere and upper atmosphere. They perturb the local densities and temperatures that affect the emission chemistry and create perturbations in the emission profiles. Figure 2.5 shows the volume emission rates as a function of height for four commonly observed unperturbed airglow emissions in the mesosphere [*Swenson et al.*, 2005; *Vargas et al.*, 2007]. It can be inferred that the emissions are not localized at a particular height and there exists a Gaussian-like shape which is a function of the neutral density and temperature

profile of the atmosphere.

Perturbations to these emission profiles by AGWs bear signatures of the underlying wave structure and can be imaged using ground-based instruments [*Viereck and Deehr*, 1989; *Zhang et al.*, 1993; *Reisin and Scheer*, 1996; *Walterscheid et al.*, 1999; *Hecht et al.*, 2001a]. The measurements made by ground-based imagers are line-of-sight integrated quantities and are, thus, suited to study waves with a vertical wavelength greater than the width of the airglow layer ($\lambda_z > 12$ km). If $\lambda_z < 12$ km, integrating across the crests and troughs will result in cancellation and will not reflect actual perturbation features. Also, to be imaged, the horizontal wavelength, λ_h, must fit within the field of view of the imager, typically less than 300 km. The airglow intensity, I, and the rotational temperature, T_R, are the two quantities that are commonly measured from ground-based instruments in order to study the perturbed airglow. I is the vertically integrated volume emission rate and T_R is the vertically integrated air temperature weighted by the profile of the volume emission rate. By studying the phase differences and amplitude fluctuations of these parameters over different airglow emission heights, parameters like λ_z can be estimated along with the vertical energy flux of the wave. In Figure 2.6 the vertical profile of a modeled unperturbed hydroxyl (OH) airglow is shown along with the perturbed structure. The thick solid curve is the average emission profile while the thin solid lines represent the airglow perturbed 5% by an AGW with a vertical wavelength of 25 km [*Swenson et al.*, 2005; *Liu and Swenson*, 2003].

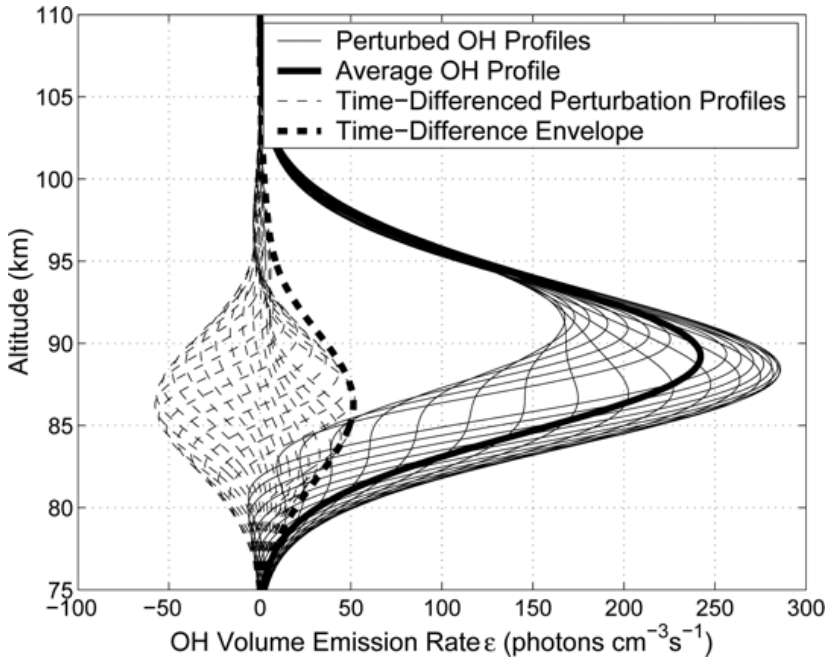

Figure 2.6 The vertical profile of a modeled hydroxyl airglow emission. The thin solid lines represent a time-sequential series, the thick solid curve represents the average emission profile, the thin dashed curves represent the time differenced perturbation profiles, while the thick dashed curve shows their envelope (after *Swenson et al.* [2005]; *Liu and Swenson* [2003]).

The following section provides a brief review of the how the vertical wavelength has been estimated in the past using two-dimensional images of the perturbed airglow emission layers.

2.4 Historical Review of the Estimation of λ_z

The first published images of the perturbed airglow [*Peterson and Kieffaber*, 1973] showed wavelike patterns of bright and dark areas as shown in Figure 2.7.

Figure 2.7 One of the first infrared images of the airglow perturbed by atmospheric gravity waves (after *Peterson and Kieffaber* [1973]).

Tremendous work has subsequently followed in developing techniques to estimate gravity wave parameters from airglow image data. Instruments like CCD imagers are used to measure fluctuations in the airglow layers instigated by gravity wave propagation. To be able to quantify the energy and momentum transported by AGWs using Equation 2.10, the unknowns are the wave amplitude, $\left(\frac{\rho_1}{\rho_0}\right)$, the vertical wavelength, λ_z, and the intrinsic frequency, ω. The measurements of the horizontal intrinsic phase speed, $c = \frac{\omega}{k}$, are biased by mesospheric winds which are hard to measure, unlike k, which can be directly measured from a single, ground-based airglow observation [*Hecht et al.*, 2001b]. In *Vargas et al.* [2007], the energy and momentum flux are calculated using a cancellation factor (CF) that relates the wave amplitude to the observed airglow imagery. The CF can be used if k_z is known. Lidars and radars can be used to directly measure either k_z or the mesospheric winds [*Taylor et al.*, 1995]. The intrinsic phase speed can be computed from wind measurements which can then be used to calculate λ_z using the dispersion relation, Equation 2.6. This technique relies on multi-instrument measurements, which may

not always be available.

To measure λ_z solely from airglow imagery, simultaneous observations of a single airglow layer from different locations on the ground can be used to tomographically reconstruct the vertical structure. *Nygren et al.* [1998] implemented a stochastic-based regularization to tomographically invert a simulated wave perturbation. *Nygren et al.* [2000] applied this method to real data and it was concluded that an array of two imagers was insufficient. In 2005, an array of three imagers set up 150-km apart, oriented along a 1-D axis, was used to compare different reconstruction techniques to tomographically image the emission perturbation from a simulated wave. It was concluded that the Tikhonov method produced the best results. In general, tomographic inversion techniques are highly dependent on the quality of the observations and can be computationally complex to solve. Thus, in order to estimate λ_z reliably, an array of ground-based imagers must be installed, which might not be always be feasible.

Besides tomography, λ_z can be estimated by correlating the phase structure seen in simultaneous measurements of multiple airglow layers that are separated in altitude. The phase on each layer is measured in its principal phase and thus there is an ambiguity whether the successive measurement is within that principal phase or the next 2π window. Therefore, this method, although conceptually simple, suffers from the 2π ambiguity. *Anderson et al.* [2009] describe a non-tomographic method to directly estimate all the intrinsic wave parameters of an AGW using airglow images of a single emission layer taken from ground-based imagers. A mathematical model of the perturbed emission layer is introduced along with how it relates to the airglow data. This thesis aims to validate the model using real data by solving the unknown parameters in the model using two parameter estimation techniques.

2.5 Conclusion

In this chapter an introductory review is presented on atmospheric gravity waves and the phenomenon of airglow. As the AGWs transport energy and momentum to the upper mesosphere, they modulate the airglow emission layers. Through observations of the perturbed airglow we can estimate the parameters of gravity waves using tomography and other techniques. A brief history of how this has been attempted in the past is subsequently furnished. In the next chapter, a model of the airglow perturbation is introduced and theory of a parameter estimation technique is developed.

CHAPTER 3

PARAMETER ESTIMATION

The vertically propagating atmospheric gravity waves that perturb the airglow emission profiles are very diverse in terms of their horizontal wavelengths and periods. In *Taylor et al.* [1997], gravity waves with λ_h ranging from 5 km to 100 km were imaged in three airglow emission layers to study their morphology and dynamics. Waves with distinct spatial and temporal properties were observed and were broadly categorized as either "bands" or "ripples." The first category is the more prominent group and the waves appear as quasi-monochromatic, exhibiting horizontal wavelengths of a few to several tens of km and lasting for a few hours. "Ripples", on the other hand, are waves with $\lambda_h \sim 6$ to 16 km [*Peterson and Adams*, 1983], and shorter lifetimes ($<$ 45 minutes) [*Peterson*, 1979]. Figure 3.1 illustrates waves that are characteristic of these two categories. Figure 3.1 (a) and (b) are bands which are quasi-monochromatic with larger wavelength and longer lifetimes than ripples, Figure 3.1 (c). Figure 3.1 (d) is a complex mixture of band and ripple waves.

The quasi-monochromaticity of the most prevalent wave structure observed can be exploited to develop a simple, yet powerful model, of the perturbed airglow. Estimation of 3-D structure from 2-D imagery lends itself nicely to parameter estimation techniques based on this model. The following sections develop the airglow perturbation model followed by a description of how the vertical wavelength may be estimated using parameter estimation.

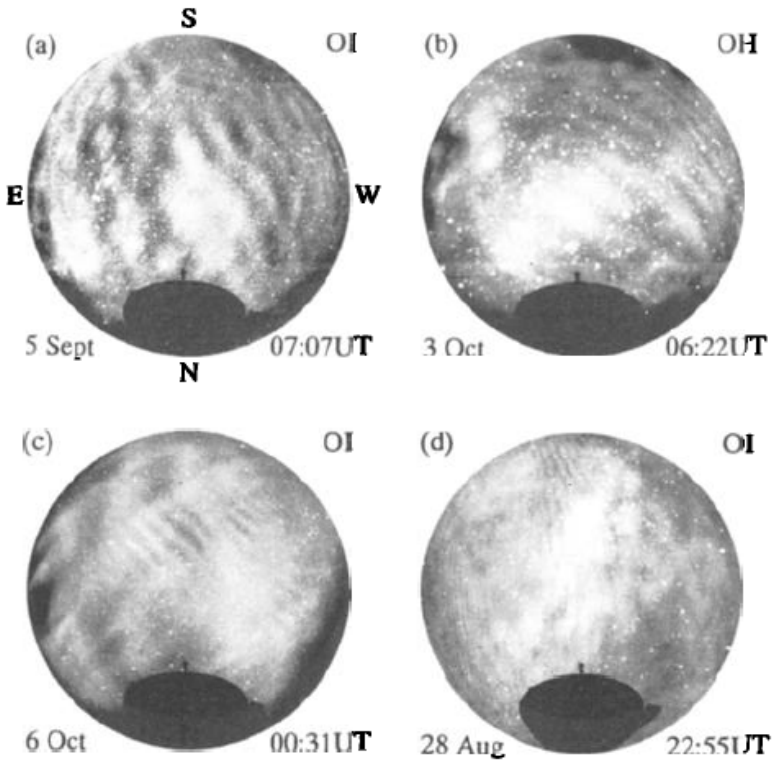

Figure 3.1 Four images showing examples of gravity wave structure recorded in the OI(557.7 nm) and near-infrared OH emissions during the campaign: (a, b) extensive bands; (c) example of transient ripples and (d) a complex mixture of band and ripple waves. Note that the oval silhouette at the bottom of each image is the Instituto Nacional de Pesquisas Espaciais satellite tracking antenna, while the dark patches at low elevations in (b) and (c) are clouds (after *Taylor et al.* [1997]).

3.1 Airglow Perturbation Model

In this chapter, we follow the airglow perturbation model developed by *Anderson et al.* [2009]. The airglow emission profile perturbed by a propagating AGW is modeled as a quasi-monochromatic (QM) wave function that is scaled in amplitude

by the vertical profile of the airglow layer, expressed as

$$V(x_r, y_r, z_r) = \frac{1}{2} A(x_r, y_r) p(z_r) \exp\left[j\left(k_x x_r + k_y y_r + k_z z_r + \omega_t t + \phi(x_r, y_r)\right)\right] + c.c. \tag{3.1}$$

where $c.c$ is the complex conjugate. As the airglow observations made by an imager are localized to a given height in the mesosphere, the horizontal co-ordinate system, (x_r, y_r) is defined at this height z_r, which is known a priori. The sinusoidal wave is spatially as well as temporally periodic. $A(x_r, y_r)$ is the horizontal amplitude function of the wave structure and $\phi(x_r, y_r)$ is the horizontal phase function which models non-idealities like unequal intensities of successive crests or curved wave fronts. In reality, the gravity waves perturbing the airglow are rarely purely monochromatic, so a spatially dependent amplitude and phase function are incorporated in the model to account for it. The term $p(z_r)$ is the vertical profile of the airglow layer, k_x, k_y and k_z are mutually orthogonal wavenumbers where $k = \sqrt{k_x^2 + k_y^2 + k_z^2}$ and ω_t is the temporal frequency of the wave. When the two-dimensional spatial Fourier transform of Equation 3.1 is taken, we get a horizontally band-limited feature in the frequency space. The bandwidth, B, is set at $\frac{2\pi}{3\lambda_h}$ implying that in the (x, y)-space the wave is monochromatic within a window that is three horizontal wavelengths large.

An expression for the data acquired by imagers can be determined by taking the line-of-sight integral of Equation 3.1 along a vector, (x', y', z'), from the imager at (x_0, y_0, z_0) to a height z_c, the centroid height of the airglow layer, $p(z)$, as shown in Figure 3.2. This is expressed as

$$g(x', y', z', x_0, y_0, z_0) = C\gamma(z') \int_{-\infty}^{\infty} V\left(\frac{x'}{z'}(z_c - z_0) + x_0, \frac{y'}{z'}(z_c - z_0) + y_0, z\right) dz, \tag{3.2}$$

where C is a constant photometric conversion factor and $\gamma(z')$ is the function along

the line-of-sight integral that incorporates the in-band atmospheric transmittance. The constant C converts a measurement of the optical radiation to a pixel value and is a property of the imager. The term $\gamma(z')$ accounts for absorption of the radiation by the line-of-sight atmosphere as well as the roll-off function of the imaging system.

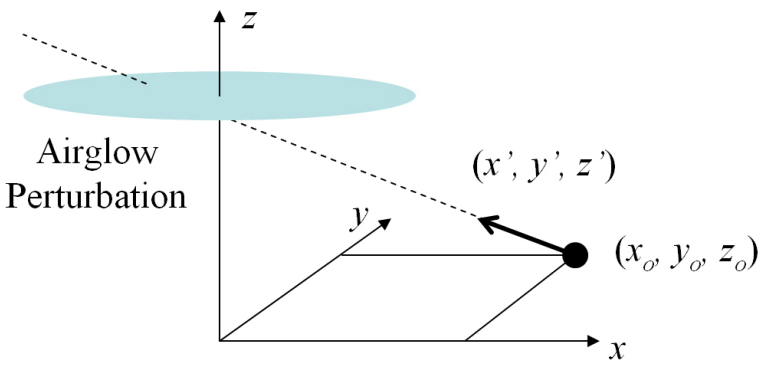

Figure 3.2 The observation geometry of the airglow layer and the imager. Here, the imager co-ordinates are (x_0, y_0, z_0) and the line-of-sight vector is (x', y', z') (after *Anderson et al.* [2009]).

The two constants, C and $\gamma(z')$, are discarded from the analysis under the assumption that they are known a priori. As the QM wave model for the perturbed airglow is band-limited, the fluctuations in $A(x_r, y_r)$ and $\phi(x_r, y_r)$ are small with respect to the vertical width of the vertical profile, $p(z_r)$. As they do not vary much along the vertical dimension, they are treated as constants while evaluating Equation 3.2. Using Equation 3.1 in Equation 3.2 and expressing the inner product of $p(z_r)$ and the complex exponential in the Fourier domain, Equation 3.2 can be written as

$$g(x', y', z', x_0, y_0, z_0) = \frac{A(x_r, y_r)}{2z'} \int\int \bar{p}(q_z) * \delta(q_z - (w + k_z)) e^{(j\alpha + jq_z z)} dq_z dz + (3.3)$$

where $\bar{p}$ is the Fourier transform of $p(z)$ and

$$\begin{aligned} w &= k_x \frac{x'}{z'} + k_y \frac{y'}{z'} \\ \alpha &= k_x x_0 + k_y y_0 - w z_0 + \omega_t t + \phi(x_r, y_r). \end{aligned}$$

Using the sifting property of the delta function, the above equation is further reduced to

$$g(x', y', z', x_0, y_0, z_0) = \frac{A(x_r, y_r)}{2z'} \bar{p}(w + k_z) e^{\jmath\alpha} + c.c. \tag{3.4}$$

Equation 3.4 implies that an imager's pixel value is represented in terms of the phase-modulated Fourier transform of the vertical profile of the airglow emission. Thus, if $p(z)$ is approximated as a Gaussian curve centered at the centroid height, z_c, and a thickness of σ, expressed as

$$p(z) = \frac{1}{\sqrt{2\pi\sigma^2}} e^{-\frac{1}{2\sigma^2}(z - z_c)^2},$$

with a Fourier transform given by

$$\bar{p}(q_z) = e^{-\frac{\sigma^2}{2} q_z^2} e^{-\jmath q_z z_c},$$

then Equation 3.4 can then be rewritten as

$$g(x', y', z', x_0, y_0, z_0) = \frac{A(x_r, y_r)}{2z'} e^{-\frac{\sigma^2}{2}(w + k_z)^2} e^{\jmath(\alpha - (w + k_z) z_c)} + c.c. \tag{3.5}$$

Equation 3.5 describes how the airglow profile perturbed by a QM gravity wave is translated to its measurement made by an imager. Each pixel value on the imager corresponds to a perturbed airglow value that is functionally expressed as a complex exponential scaled by a Gaussian. Thus, each imager pixel value has information about the vertical wavelength embedded in its magnitude and phase,

as seen in Equation 3.5. Before we proceed with the estimation of the parameters of interest, Equation 3.5 can be further reduced by eliminating its dependence on the van Rhijn effect. The van Rhijn effect [*Nygren et al.*, 2000] is the increase in airglow intensity with increasing zenith angle and the line-of-sight vector. This effect can be eliminated by multiplying both sides of Equation 3.5 by z'. Airglow data collected from collocated systems have different line-of-sight measurements of the intensity. Thus, in order to analyze the images in a unified co-ordinate system, the data at the imager location (x_0, y_0, z_0) must be projected onto a plane having horizontal co-ordinates (x, y) at an altitude of H kilometers. Statistically, the airglow emission profile is well studied and the value of $H \approx z_c$. Figure 3.3 shows raw images of the airglow emission at a center frequency of 557.7 nm, known as the greenline emission, that is perturbed by a propagating AGW. Figure 3.3 (a) and (b) are taken from optical imagers installed at Socorro and the National Solar Observatory both in New Mexico. Figure 3.3 (c) and (d) are obtained by geometrically transforming the two images to a common unified co-ordinate system.

Incorporating the van Rhijn effect and projecting the data into the H-altitude layer, Equation 3.5 can be expressed as

$$g(x,y) = \frac{A(x,y)}{2} e^{-\frac{\sigma^2}{2}(w_i(x,y)+k_z)^2} e^{\jmath(\beta(x,y)+(z_c-H)w_i(x,y))} + c.c., \tag{3.6}$$

where

$$\begin{aligned} w_i(x,y) &= w \\ &= k_x \frac{x-x_0}{H-z_0} + k_y \frac{y-y_0}{H-z_0} \\ \beta(x,y) &= k_x x + k_y y + k_z z + \omega_t t + \phi(x,y). \end{aligned} \tag{3.7}$$

Equation 3.6 represents the pixel value of a ground-based imager measuring AGW-

perturbed airglow emission. It is dependent on the spatial and temporal frequencies apart from the point in the projected image space that is being observed. Moreover, the unknown vertical wavelength, λ_z, is embedded in the phase and magnitude of the pixel value. In the following section, a filtering technique, called Gabor filtering, is described that isolates the phase and magnitude of Equation 3.6, which is then used to independently estimate the vertical structure of the AGW.

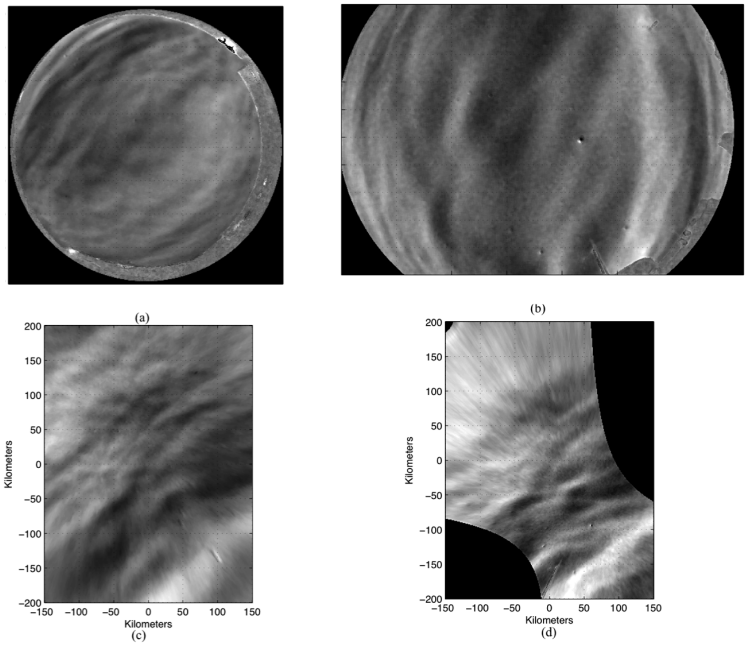

Figure 3.3 (a), (b) Optical images from Socorro and the National Solar Observatory in New Mexico. (c), (d) Geometric transformation of (a) and (b) to a common unified co-ordinate system.

3.2 Gabor Filtering

The measurements of the perturbed airglow have an associated bandwidth due to the QM nature of the AGWs. The Fourier transform of the model in Equation 3.6 will be a two-dimensional spatial Gaussian function that is centered at the spatial frequencies (k_x, k_y) along with its complex conjugate term centered at $(-k_x, -k_y)$,

as illustrated in Figure 3.4.

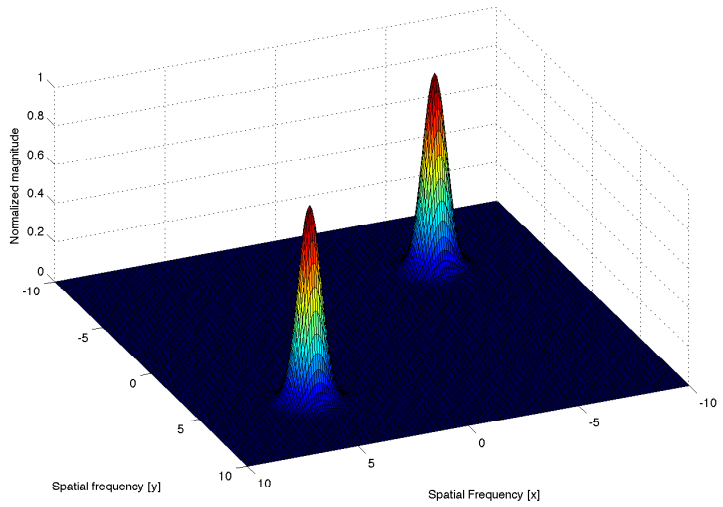

Figure 3.4 The Fourier transform of the model in Equation 3.6 will be a two-dimensional spatial Gaussian function that is centered at the spatial frequencies (k_x, k_y) along with its complex conjugate term centered at $(-k_x, -k_y)$.

A bandpass Gaussian filter, called the Gabor filter, is subsequently applied to the model such that the model's bandwidth falls within the pass-band of the filter and thus eliminates the complex conjugate term, thereby reducing Equation 3.6 to the following:

$$g(x,y) * *h(x,y,q_x,q_y) = \frac{A_{xy}}{2} e^{-\frac{\sigma^2}{2}(w_i(x,y)+k_z)^2} e^{\jmath(\beta(x,y)+(z_c-H)w_i(x,y))}. \tag{3.8}$$

Thus, the airglow emission perturbed by a QM AGW is expressed as a two-dimensional Gaussian function that is shifted in frequency-space by an amount proportional to the horizontal frequencies k_x and k_y. The term $h(x,y,q_x,q_y)$ is the mathematical expression for the Gabor filter and is expressed as

$$h(x,y,q_x,q_y) = \frac{1}{\pi T^2} e^{\frac{1}{2T^2}(x^2+y^2)+\jmath(q_x x+q_y y)}, \tag{3.9}$$

where q_x and q_y are the spatial frequencies of the two-dimensional Gaussian and

$$T = \left(\frac{4\pi^2}{q_x^2 + q_y^2} \right)^{\frac{1}{2}}. \tag{3.10}$$

In the frequency-space the Gabor filter is a Gaussian-shaped band-pass filter centered at (q_x, q_y). Its bandwidth and center frequency are determined by setting two parameters T and θ. T, as in Equation 3.10, is related to the horizontal spatial frequency and describes the bandwidth of the Gabor filter,

$$B_f \approxeq 0.374 \frac{2\pi}{T}.$$

$\theta = \arctan\left(\frac{q_y}{q_x}\right)$ is related to the slope of the wavefronts in (x, y) space as seen in the airglow images and thus describes the spatial spread of the Gabor filter in the frequency-space. By setting different values for T and θ, a unique Gabor filter can be realized with desired pass-band characteristics as illustrated in Figure 3.5.

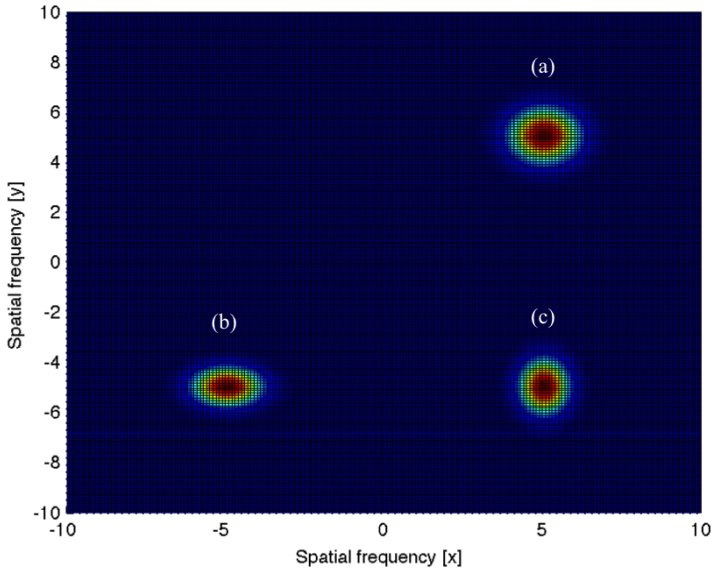

Figure 3.5 The spectral response of the Gabor filter is plotted when q_x and q_y are equal (a), $q_x > q_y$ (b) and $q_x < q_y$ (c).

In the figure, the spectral response of the Gabor filter is plotted when q_x and q_y are equal (a), $q_x > q_y$ (b), and $q_x < q_y$ (c). Figure 3.6 summarizes the process of Gabor filtering that starts with a projected image of the perturbed airglow, denoted by $g(x, y)$, that is convoluted in two dimensions with the Gabor filter, $h(x, y, q_x, q_y)$, as expressed in Equation 3.8. When $q_x = k_x$ and $q_y = k_y$ and $T = \lambda_h$, the filter is matched and each pixel in the filtered image has a complex value as per Equation 3.8. Figure 3.6 shows the magnitude of the filtered image which resembles a Gaussian implying a good fit between the data and the filter.

In order to determine the unique parameters, T and θ, for the Gabor filter, a point near the center of the magnitude of the filtered image is chosen and plotted for a range of T and θ values. By choosing a point near the center, we attempt to quantify the degree of fit of the filter with the data. A well-fit filter will efficiently eliminate the c.c. term and the chosen point will sample the peak of the Gaussian. If the Gabor filter does not match the characteristics of the AGW perturbing the airglow, then aliasing will occur resulting in multiple peaks from the superposition of the various signals. Figure 3.7 shows an example of a filter bank obtained after filtering airglow images for a whole night with different values of T and θ. The Gabor parameters corresponding to the region where the intensity is maximum are chosen.

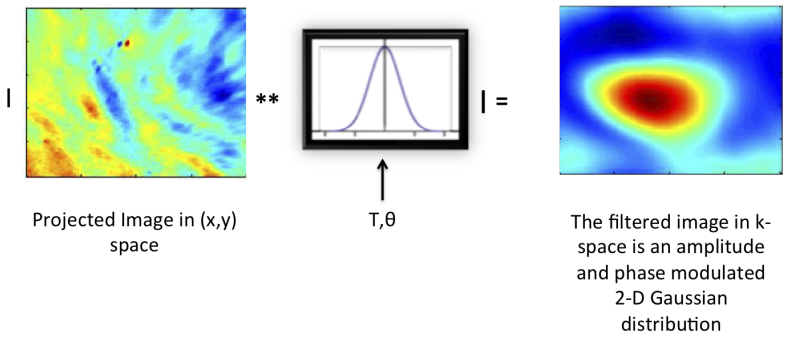

Figure 3.6 Equation 3.8 illustrated. The magnitude of the filtered image resembles a Gaussian indicating that the Gabor filter is matched to the AGW characteristics.

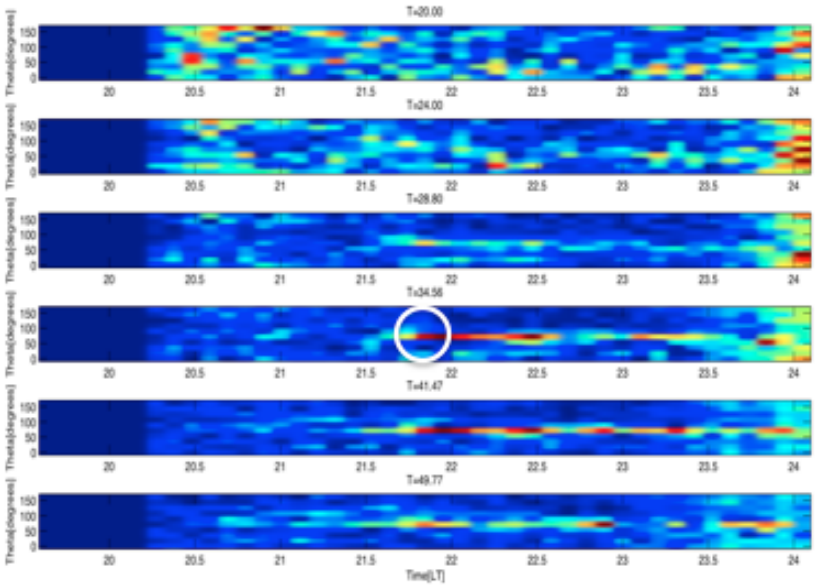

Figure 3.7 A filter bank obtained after filtering airglow images for a whole night with different values of T and θ. The parameters for the Gabor filter, T and θ, corresponding to the region where the intensity is maximum is chosen, indicated here by a white circle.

The following section introduces two techniques to estimate the unknowns in Equation 3.8 by analyzing the phase and magnitude of the filtered image.

3.3 Parameter Estimation

Each pixel on the filtered image is a complex value representing the real and the imaginary parts of Equation 3.8. The vertical wavelength, λ_z, is the parameter that has to be estimated so as to quantify the vertical energy and momentum flux transport by AGWs into the upper layers of the mesosphere. As the phase and magnitude of Equation 3.8 are functions of λ_z, two independent estimation techniques are developed to determine λ_z.

3.3.1 Phase Analysis

The phase of Equation 3.8 is expressed as

$$\angle G(x,y) = k_x x + k_y y + k_z z + \omega_t t + \phi(x,y) + (z_c - H)\omega_i(x,y). \tag{3.11}$$

Under the assumption that the airglow emission profile is well-studied such that the height of the altitude layer in which the images are projected, H, coincides with the centroid of the airglow emission profile, z_c, the last term in Equation 3.11 is eliminated. For a given pixel value, (x, y), in the projected image space, the horizontal frequency terms, $k_x x$ and $k_y y$, are simply constants and the phase fluctuation function, $\phi(x, y)$, is an unknown. The temporal frequency, ω_t, of the wave is also an unknown parameter along with the vertical wavelength, λ_z, manifested as the vertical spatial frequency term, $k_z z$, in Equation 3.11. Equation 3.11 can be reduced to

$$\angle G(x,y) = k_z z + \omega_t t + \phi(x,y). \tag{3.12}$$

The three unknowns, $\lambda_z, \omega_t, \phi(x, y)$, can be solved by using, at the minimum, three linearly independent equations. In the presence of measurements with uncertainties, solving an overdetermined system of equations, where the equations are more than the number of unknowns, will lead to improved estimates of the unknowns. To achieve this, the optical imagers make measurements of three different airglow emissions at three time instances. As the different airglow emissions are localized at different heights, z, in the mesosphere we are able to define a linearly independent

system as expressed in the following form:

$$\begin{bmatrix} \angle G_1^1 \\ \angle G_2^1 \\ \angle G_3^1 \\ \angle G_1^2 \\ \angle G_2^2 \\ \angle G_3^2 \\ \angle G_1^3 \\ \angle G_2^3 \\ \angle G_3^3 \end{bmatrix} = \begin{bmatrix} z_1 & t_1^1 & 1 \\ z_1 & t_2^1 & 1 \\ z_1 & t_3^1 & 1 \\ z_2 & t_1^2 & 1 \\ z_2 & t_2^2 & 1 \\ z_2 & t_3^2 & 1 \\ z_3 & t_1^3 & 1 \\ z_3 & t_2^3 & 1 \\ z_3 & t_3^3 & 1 \end{bmatrix} \times \begin{bmatrix} k_z \\ \omega_t \\ \phi(x,y) \end{bmatrix}. \tag{3.13}$$

$$\mathbf{b} = \mathbf{A} \times \mathbf{x}$$

Equation 3.13 describes the system of equations expressed in its matrix notation followed by its symbolic representation. The left-hand side of this equation represents the measurements of the phase of the filtered image at a particular point in (x, y) space. The superscript of $\angle G_t^z$ indicates which airglow emission layer the measurement is made in while its subscript indicates its time. The system in Equation 3.13 is solved by regressing b on $A \times x$ to minimize $\|A \times x - b\|$ in the least squared sense. The minimization process is realized by equating the first derivative of the minimization function, $\|A \times x - b\|$, to zero, to get a set of simultaneous linear equations in the unknown parameters, x. These equations are known as the normal equations and can be solved to yield the parameter estimates.

3.3.2 Magnitude Analysis

The magnitude of the filtered image, as in Equation 3.8, is a two-dimensional Gaussian expressed as

$$|G(x,y)| = A(x,y)e^{-\frac{\sigma^2}{2}(\omega_i(x,y)+k_z)^2}. \tag{3.14}$$

The magnitude of the filtered image is a function of the width of $p(z)$, σ, that is well-modeled and known beforehand. Also, the term $\omega_i(x,y)$ is constant for a given point in the projected image space (x,y) of the filtered image as described by Equation 3.7. The unknown amplitude fluctuation, $A(x,y)$, and λ_z have a non-linear relationship with the magnitude of the filtered image and are estimated using the Newton-Raphson algorithm. The Newton-Raphson algorithm for a function $f(x)$ finds the zero of the function by iterating through a set of points that eventually converge to the root. The choice of successive estimates in the iterative process is derived from the definition of a derivative. The derivative of a function, $f(x)$,

$$f'(x_n) \quad = \quad \frac{\triangle y}{\triangle x} = \frac{f(x_n)-0}{x_n - x_{n+1}},$$

can be rearranged to relate the current estimate to the next estimate in the iteration as

$$x_{n+1} = x_n - \frac{f(x_n)}{f'(x_n)}.$$

The process is illustrated in Figure 3.8, where x_{n+1} is the $x-$intercept of the slope of the function at x_n.

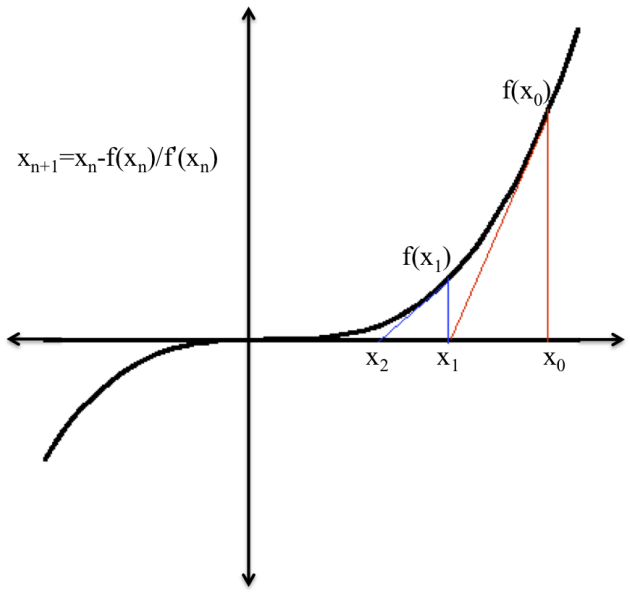

Figure 3.8 The Newton-Raphson algorithm for a function $f(x)$ finds the zero of the function by iterating through a set of points that eventually converge to the root.

A number of issues arise for methods based upon the derivative of a function. Firstly, if the derivative of the function is not continuous in the neighborhood of the root, then the method may diverge as division by a small number or zero will result in overshoot and non-convergence. Convergence may also fail if the initial estimate is far from the root.

In its simplest case, the unknowns in Equation 3.14 can be estimated by choosing a single point in the (x, y) space of the projected images taken from two imagers measuring perturbations of the same airglow emission layer. Since the amplitude fluctuation function, $A(x, y)$, is dependent on (x, y), the single point on the airglow perturbation observed by two imagers should have the same value; the other unknown is λ_z. Also, we will have two different measurements of $|G(x, y)|$ from the filtered image at the point (x, y) on the two imagers. Thus, there are two unknowns in two equations which can be solved by making an initial estimate for $A(x, y)$ and

λ_z, followed by iterating to the actual values using the Newton-Raphson algorithm. It is advantageous to solve an overdetermined system where the number of observations is more than the unknowns in order to eliminate possible bias in an observation point. Therefore, if there are N imagers and M data points on each imager, the number of observations of $|G(x,y)|$ is $M \times N$ while the number of unknowns is $M+1$ (M different values of $A(x,y)$ and one unique λ_z). This will entail making $M+1$ initial guesses in the Newton-Raphson algorithm to iteratively solve for the following system:

$$\bar{x}_{n+1} = \bar{x}_n - J^{-1}\bar{f}(x_n), \tag{3.15}$$

where J is the Jacobian matrix of all first-order partial derivatives of a vector- or scalar-valued function with respect to another vector. For magnitude analysis, Equation 3.15 is expanded

$$\begin{bmatrix} \lambda_{z,n+1} \\ A(x,y)^1_{n+1} \\ A(x,y)^2_{n+1} \\ . \\ . \\ A(x,y)^M_{n+1} \end{bmatrix} = \begin{bmatrix} \lambda_{z,n} \\ A(x,y)^1_n \\ A(x,y)^2_n \\ . \\ . \\ A(x,y)^M_n \end{bmatrix} - J^{-1} \times \begin{bmatrix} |G(x,y)|^1 - Z^1_n \\ |G(x,y)|^2 - Z^2_n \\ |G(x,y)|^3 - Z^3_n \\ . \\ . \\ |G(x,y)|^{M\times N} - Z^{M\times N}_n \end{bmatrix}, \tag{3.16}$$

where the Jacobian matrix, J, is given as

$$J = \begin{bmatrix} \frac{\partial Z_n^1}{\partial \lambda_z} & \frac{\partial Z_n^1}{\partial A(x,y)^1} & . & . & \frac{\partial Z_n^1}{\partial A(x,y)^M} \\ \frac{\partial Z_n^2}{\partial \lambda_z} & \frac{\partial Z_n^2}{\partial A(x,y)^1} & . & . & \frac{\partial Z_n^2}{\partial A(x,y)^M} \\ \frac{\partial Z_n^3}{\partial \lambda_z} & \frac{\partial Z_n^3}{\partial A(x,y)^1} & . & . & \frac{\partial Z_n^3}{\partial A(x,y)^M} \\ . & . & . & . & . \\ . & . & . & . & . \\ \frac{\partial Z_n^{M\times N}}{\partial \lambda_z} & \frac{\partial Z_n^{M\times N}}{\partial A(x,y)^1} & . & . & \frac{\partial Z_n^{M\times N}}{\partial A(x,y)^M} \end{bmatrix}. \tag{3.17}$$

In Equation 3.16, the slope is approximated by the error function that is the difference between $|G(x,y)|$ and its estimate at the nth-iteration, Z_n, which is computed using Equation 3.14 with values of $A(x,y)_n$ and λ_n. The Newton-Raphson is iterated until the system satisfies a stated error-bound given by the difference between the model, Z_n, and the data, $|G(x,y)|$. Once this error function is minimized the estimate of λ_z can be compared to that computed from the phase of Equation 3.8.

3.4 Conclusion

In this chapter, Anderson's model for a perturbed airglow emission layer as measured by a ground-based imager is derived. The perturbed airglow is modeled as a quasi-monochromatic wave whose amplitude is modulated by the unperturbed airglow emission profile. A band-pass filter, known as the Gabor filter, is chosen with a center frequency and passband characteristics that eliminate the complex conjugate term of the perturbed airglow when represented in the Fourier domain. Thus, each pixel on the filtered image is complex valued with λ_z embedded in its phase and magnitude, as expressed by Equation 3.8. Two parameter estimation techniques are introduced that are applied on the phase and magnitude to independently estimate λ_z. The next chapter describes an experiment setup in New Mexico to observe

AGWs followed by results of the parameter estimation process applied on the data collected from it.

CHAPTER 4

DATA ANALYSIS

In this chapter, the instrumentation deployed for an experiment to make ground-based observations of AGWs is described. The instrumentation comprises two co-located ground-based imagers making coincident measurements of multiple airglow layers. The first imager is located at Socorro, New Mexico, 150 miles from the second which is installed at the National Solar Observatory in Sunspot, New Mexico. Once the imager data is processed with the Gabor filter, each pixel in the filtered image is complex valued, with a phase and magnitude that relate to λ_z through Equation 3.11 and Equation 3.14 respectively. The two parameter estimation techniques discussed in Chapter 3 are applied to the data; each produces similar estimates of λ_z, suggesting the validity of the model. After a description of the instrumentation, some pre-processing steps are discussed followed by a presentation of the results of the parameter estimation techniques for a few nights.

4.1 Instrumentation

In the summer of 2010, two ground-based imagers were set up in New Mexico to make coincident observations of multiple airglow layers in the mesosphere. The first imager was installed at the National Solar Observatory (NSO) in Sunspot, New Mexico, with a latitude and longitude of 32.79°N/105.81°W. The imager was

placed in a metallic crate with a circular opening on the top face that was fitted with a hemispherical plastic dome. The objective lens of the all-sky CCD imager was set parallel to the base of this hemisphere. Light entering through the objective lens is passed through an optical filter and then focussed onto the CCD sensor array. The imager provides a field of view of 140°. There are four optical filters housed in a rotating mechanical wheel that is powered by an electric motor. The four optical filters are observing the background continuum (551.1 nm), greenline (557.7 nm), redline (630.0 nm) and the O_2 (865.5 nm) emissions. The transmission characteristics of each optical filter will affect the amount of light received on the CCD sensor array. Another set of optics refocusses the light onto the CCD sensor array. The CCD sensor array is rectangular with dimensions 490 x 728 pixels, 3 x 3 binning and a gain of 12. While the readout noise is mitigated by binning, the dark current and thermal noise are reduced by a liquid cooling unit that cools the CCD to -30° C.

A second imager was installed in Socorro, New Mexico, 34.05°N/106.92°W. It is vertically mounted on a set of rails that are bolted on the inside wall of a trailer, as shown in Figure 4.1. Just like the imager at NSO, there are basically three components of this imager - the objective lens, the filter wheel and the CCD sensor array. The objective lens, at the top, with a field of view of 180°, screws on to the filter wheel whose bottom side is friction fit with a black cylindrical metallic tube that is aligned over another set of focussing optics and the CCD. Both the lenses on this imager have their apertures opened all the way to maximize the input signal. The filter wheel houses four optical filters - the background (551.0 nm), greenline (557.7 nm), redline (630.0nm) and OH. The CCD sensor array is square with dimensions 512 x 512, 2x2 binning and a gain of 1. The CCD is electronically cooled to -35° C.

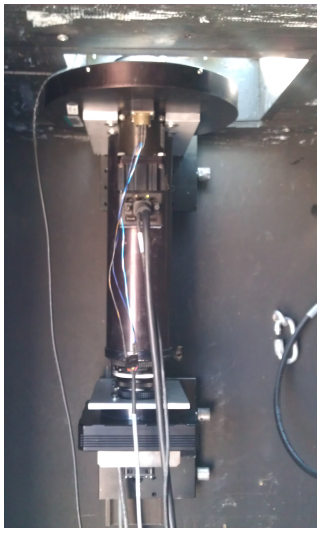

Figure 4.1 The imagers at Socorro and NSO have three components - the objective lens, the filter wheel and the CCD sensor array. The objective lens, at the top, with a field of view of 180°, screws on to the filter wheel whose bottom side is friction fit with a black cylindrical metallic tube that is aligned over another set of focussing optics and the CCD.

Both the imagers are interfaced to a computer system through which they acquire images throughout the night. At NSO, the computer system consists of a laptop, that is connected to the internet, along with a web power switch that powers the cooler, laptop and the imager. The laptop runs a Linux environment along with software to rotate the filter wheel, acquire and read out images, schedule operations like switching on/off the cooler/CCD and transfer the data to a server. The scheduling also incorporates the rise and set times of the sun and moon to ensure that the imager exposes the CCD only past their set times. If not done so the CCD will saturate as it is very sensitive. As the computer system is connected to the internet, it can be accessed remotely to update the software or manually ride the system. The software is written in C++ and the scripts are written in perl.

The computer system for the Socorro imager is set up slightly different than

the one at NSO. It consists of a desktop and a laptop. The desktop runs a Linux environment with similar software for acquiring images, scheduling and transferring data to the server, as the system at NSO. This filter wheel, unlike the one at NSO, does not keep record of the position of each optical filter, and thus a function was written to achieve that. The Hall effect sensor is a transducer that varies the output voltage in response to a magnetic field. On the inside of the filter wheel there exists a Hall-effect sensor which responds to a magnet attached on the frame where the optical filter would screw in. Thus, as this filter nears the sensor, a change in the output voltage is read off by the software using a serial to USB converter cable. The desktop is connected on a local area network to the laptop and is running a Windows environment. The laptop connects the site to the internet through a cellular modem. It is also running an application through which the laptop can be remotely accessed. This application provides an easy way to remotely update software and override the system if needed. Through a Linux emulator for Windows called Cygwin, installed on the laptop, commands can be remotely sent to control the imager and cooler.

Throughout the course of the night, the two imagers acquire images of different airglow emission layers with different properties. The optical filter measuring the greenline emission has a transmission spectrum whose center frequency is at 557.7 nm with a bandwidth of around 3 nm. The second optical filter is a narrowband band-pass filter with a center frequency of 551.1 nm. Its purpose is to observe the background that is used to preprocess the images of the greenline emission. Thus, with observations of the background, we can make accurate measurements at the greenline layer. The optical filter measuring the redline emission is used primarily to observe structures in the ionosphere and is not used in this study. The optical band-pass filter centered at 865.5 nm measures the O_2 emission while a broadband filter measures the OH emission. The transmission characteristics of each optical filter, observing the different emission layers, will affect the amount of light received on

the CCD sensor array. The OH filter has the highest transmittance and is exposed for a shorter period (60 seconds) than the others (90 seconds). It is assumed that the AGW being observed does not change structure at these time scales. After each exposure, the filter wheel rotates to align the next optical filter with the CCD and this process continues through the night.

Data from the two imagers are used towards the two analysis techniques described in Section 3.3. For the phase analysis, measurements from multiple airglow layers are used, where observations at multiple heights are needed to construct the independent system of linear equations in Equation 3.13. Measurements of the OH from Socorro, O_2 from NSO and the greenline emission are used to observe AGW structure at 87 km, 92 km and 94 km respectively. On the other hand, the magnitude of the model, as expressed by Equation 3.14, is not linearly related to the height of the measurement, z; therefore observations of a single emission layer can be used towards estimating λ_z. Images of the greenline emission layer are used as they can be pre-processed with the measured background emissions to obtain accurate observations of AGWs. The accuracy of the magnitude analysis is significantly improved by increasing the number of imagers. An increase in observational spatial diversity will eliminate the component of the error biased from a single imager observation.

Temporally coincident measurements are also critical to the success of the estimation process as the AGW structure varies with time. The position of each optical filter on the filter wheel is known by the software controlling the imagers. A sequence to rotate the filter wheel is devised such that measurements of the same emission layer are made at the same time by the two imagers. These times are synchronized by referencing them to the Coordinated Universal Time (UT) standard, i.e., 6 hours ahead of the local time (LT) in New Mexico. As the measurements of the 557.7-nm emission are used for both the analysis techniques, images of this

layer are taken at a higher frequency than the rest. For the data acquired in 2010, the imagers were not synchronized, as a result of which images of clear nights with AGW structure were largely unusable due to lack of coincident data. Temporal synchronicity was implemented in 2011 for the two imagers by updating the software running on the computer systems. In summary, for the magnitude analysis coincident measurements of the greenline emission from both the imagers are used, while the phase analysis uses measurements of the OH from Socorro, O_2 from NSO and the greenline emission. The next section describes the preprocessing steps on the images followed by a discussion of results.

4.2 Preprocessing

Over the course of a night, the two imagers acquire data in moon and sundown conditions. Light from nearby cities or other man-made structures far in the horizon saturates the pixels at the edge of the CCD sensor array. These effects can be mitigated by applying masking tape to the area of the dome facing these sources. The passage of clouds through the field of view may result in saturation of the CCD as they reflect stray light sources in the field of view; thus large cloud cover results in bad data.

For the magnitude analysis, the background image is subtracted from each greenline image and the result is then spatially median filtered. This is followed by summing all images over the course of a night and dividing by the total number, resulting in an average image for the night. This average image is used to normalize the image data acquired from the two imagers to accommodate for differing sensitivities in the CCD sensor array. Figure 4.2 illustrates the process of subtraction of the background, Figure 4.2(b), from the raw image, Figure 4.2(a), followed by median filtering and normalization by the average image of the night, Figure 4.2(c). This

image, Figure 4.2(a), was acquired by the NSO imager on 15 May 2010 at 06:33:15 UT.

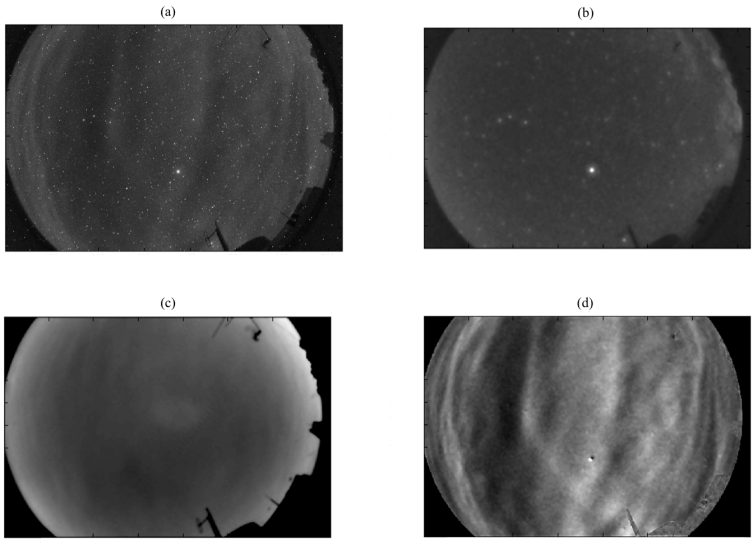

Figure 4.2 (a) Greenline emission at 557.7 nm acquired by the NSO imager on 15 May 2010 at 06:33:15 UT. (b) Image of the background that is closest taken immediately after. (c) Average image of the night that is used to normalize the background subtracted raw image to correct for differing sensitivities of the two imagers. (d) Result of this process.

For the phase analysis, the images of the OH and O_2 are median filtered. In median filtering, a sample window size is chosen and each pixel in the filtered image has a value that is the median of the pixel values in this window. The size of this window is chosen empirically for the two imager datasets. Median filtering will aid towards removing stars and other stellar phenomena seen in these images.

4.3 Results

Results of the parameter estimation techniques using the magnitude and phase of the airglow perturbation model are presented. The vertical wavelength, λ_z, estimated from the two methods on each individual night compare well to each other.

4.3.1 15 May 2010

For the night of 15 May 2010, the imagers at NSO and Socorro observed an AGW signature across the greenline, OH and O_2 airglow emission layers around 06:30 UT. The raw airglow image of the perturbed greenline emission layer taken from NSO is shown in Figure 4.3(a) and from Socorro in Figure 4.3(b).

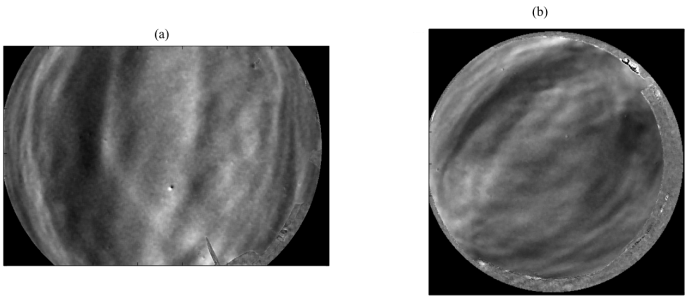

Figure 4.3 The raw airglow image of the perturbed greenline emission layer taken from NSO (a), and Socorro (b), at 06:33:15 UT.

These images are the normalized and background subtracted images with AGWs propagating through the fields of view. In order to compare the two images in a unified co-ordinate system, a geometric transformation is performed on each pixel to project the image to the centroid of the emission layer at 94.3 km. Figure 4.4 spans through a series of projected images taken from the two imagers, showing the propagation of the wavefronts in the northwest direction. It can also be observed that the resolution becomes poorer for the pixels that are farther from the imager.

This degradation is seen to the bottom right in the Socorro images and at the top left for the NSO images. The regions at the top right and bottom left of the NSO images have no data. This is because the CCD is rectangular for the NSO imager and the top and bottom regions in the raw images are cut off.

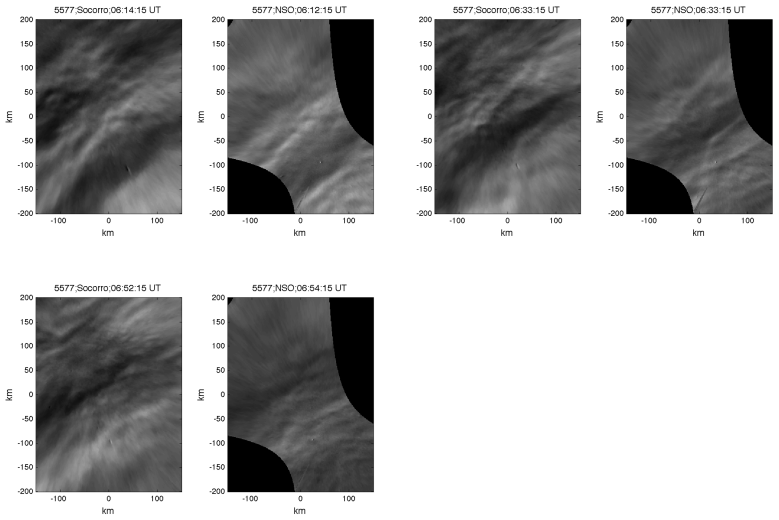

Figure 4.4 A series of projected images of the greenline emission layer taken from the two imagers, showing the propagation of the wavefronts in the northwest direction.

In order to determine the parameters, T and θ, of the Gabor filter, to eliminate the complex conjugate term, an exhaustive search is executed. The projected images of the perturbed greenline layer, taken from NSO, are Gabor filtered with T ranging from 20 to 50 and θ ranging from 0 to 180°. The magnitude of the output at the center, (0,0), is plotted. A high magnitude will indicate a well matched filter. Figure 4.5 plots this point on the filtered image for varying T, θ and time. The initial search space for T is progressively narrowed and the Gabor parameters determined are $T = 46$ km and $\theta = 128°$.

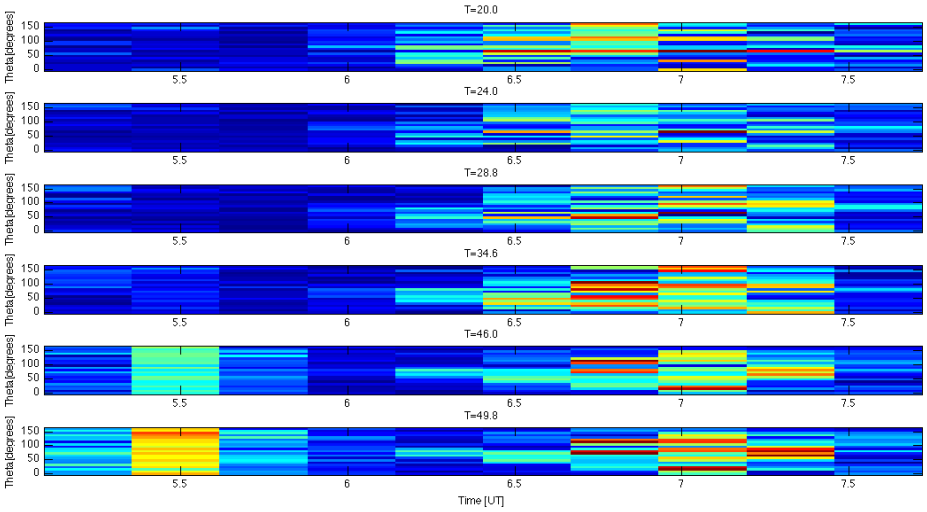

Figure 4.5 The projected images of the perturbed greenline layer, taken from NSO, are Gabor filtered with T, ranging from 20 to 50 km, and θ, ranging from 0 to 180°. The magnitude of the output at the center, (0,0), is plotted. A high magnitude will indicate a well matched filter.

The Gabor filter with these parameters is applied on the projected greenline images acquired by the two imagers at 06:33:15 UT. This particular time is chosen as there is coincident data available with parallel wavefronts propagating through the center of the images. The magnitude of the filtered images is shown in Figure 4.6. These images resemble a Gaussian function, which is expected as the mathematical expression is given by Equation 3.14.

Another repercussion of having no data at the edges is seen in the filtered NSO image. In this image it seems like there is aliasing that would be expected from an unmatched Gabor filter; however, the peaks at the edges are an effect of filtering in the spectral domain.

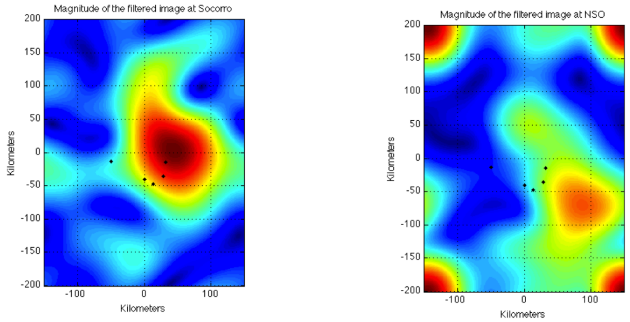

Figure 4.6 The magnitude of the filtered image where the filter parameters T and θ are matched to the spatial frequencies of the observed AGW. $T = 46$ km and $\theta = 128°$.

The five black dots in Figure 4.6 signify the points chosen for the magnitude analysis. Five points are chosen with the co-ordinates (-50, -14), (29, -36), (0, -40), (32, -15) and (14, -48) on both the imagers giving a total of ten measurements of $|G(x, y)|$. Initial guesses for the five unknown $A(x, y)$ and one λ_z are made where the next value is determined using the Newton-Raphson algorithm as described in Section 3.2. Figure 4.7 shows the result after the final iteration of this process. Each of the five Gaussian curves, represented by dotted lines, correspond to the five Z_n, represented by black dots, where $Z_n = A(x, y)_n e^{-\frac{\sigma^2}{2}(\omega_i(x,y)+k_{z,n})^2}$. The data, $|G(x, y)|$, are plotted over the model, Z_n, and it is seen that the model fits the data well with $\lambda_z = 64.6$ km.

By choosing five different points, the estimate for λ_z changes along with the fit of the model and data. The fit can be quantified by the mean squared error between Z_n and $|G(x, y)|$. A function is devised which is related to the fit, the noise in measurements and the deviation from the expected values of λ_z (λ_z is expected to fall within a range of 1 to 100 km).

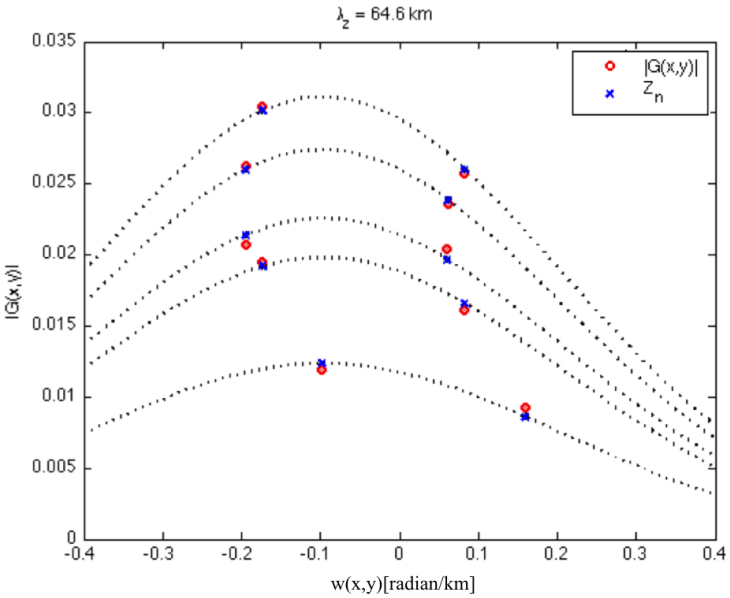

Figure 4.7 The five points chosen have the co-ordinates (-50, -14), (29, -36), (0, -40), (32, -15) and (14, -48) on both the imagers giving a total of ten measurements of $|G(x, y)|$. The data, $|G(x, y)|$, is plotted over the model, Z_n, and it is seen that the model fits the data well with $\lambda_z = 64.6$ km.

Each of these constraints are normalized and weighted, and points are chosen to minimize this function. Performing an exhaustive search on the spatial sample space for the optimal five points is not feasible. For example, if the search space is 10,000 points large, there is a total of $10,000 \times 9,999 \times 9,998 \times 9,997 \times 9,996 \approx 10^{20}$ possibilities. Thus, a local minimum is found by holding four of these five points constant and finding the fifth point that minimizes this function. Then, the first three and the fifth point are held constant to find a new fourth point that minimizes the function. This process continues until five points are found that satisfy all the constraints. The result of the process is illustrated in Figure 4.8 for a single point, (64,-17), that is improved to (69,-13) as the function is minimized.

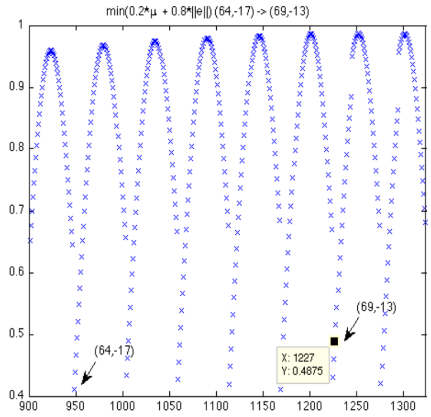

Figure 4.8 A local minimum is found by holding four of five points constant and finding the fifth point that minimizes the function. Then, the first three and the fifth point are held constant to find a new fourth point that minimizes the function. This process continues till five points are found that satisfy all the constraints. The figure shows how a single point, (64,-17), is improved to (69,-13) as the function is lower there.

For the phase analysis, three nearly coincident images of three perturbed airglow emission layers from the two imagers are used to construct a linearly independent system of equations. Table 4.1 lists the timestamps of the images chosen for the analysis.

Table 4.1 Timestamps of the images used for phase analysis, 15 May 2010

Emission	Height (km)	t_1 (UT)	t_2 (UT)	t_3 (UT)
Greenline	94.3	06:25:15	06:33:15	06:39:15
O_2	92.1	06:29:15	06:36:15	06:42:15
OH	86.8	06:26:15	06:32:15	06:38:15

A pixel at (-9,56) on all the images is chosen and the phase of the Gabor, $\angle G(x, y)$, is regressed on the unknowns λ_z, $\phi(x, y)$ and ω_t as described in Section

3.1. $\angle G(x, y)$ of a pixel is in its principal phase and thus has to be unwrapped as two values of the phase that are close to each other could be separated by 2π. To remove this ambiguity, the phase is examined at each emission layer to determine if the phase observed in successive time instances are on successive wavefronts. This is illustrated in Figure 4.9, where the phase of the greenline emission is plotted for the three time instances. A factor of 2π is added to $\angle G(x, y)$ at the third time instance as the wave has propagated a full phase.

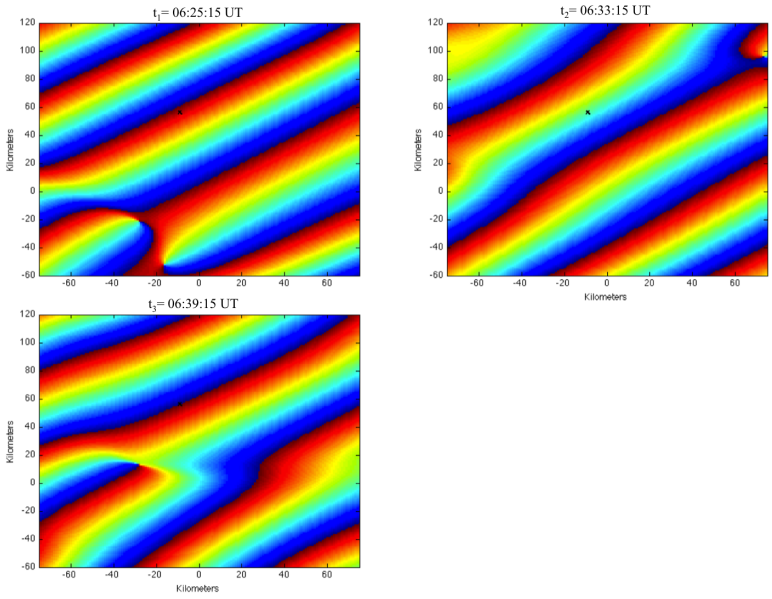

Figure 4.9 As the phase is in its principal phase it must be unwrapped before solving the system of equations. The phase of the greenline emission is plotted for three time instances . A factor of 2π is added to $\angle G(x, y)$ of the third time instance as the wave has propagated a full phase.

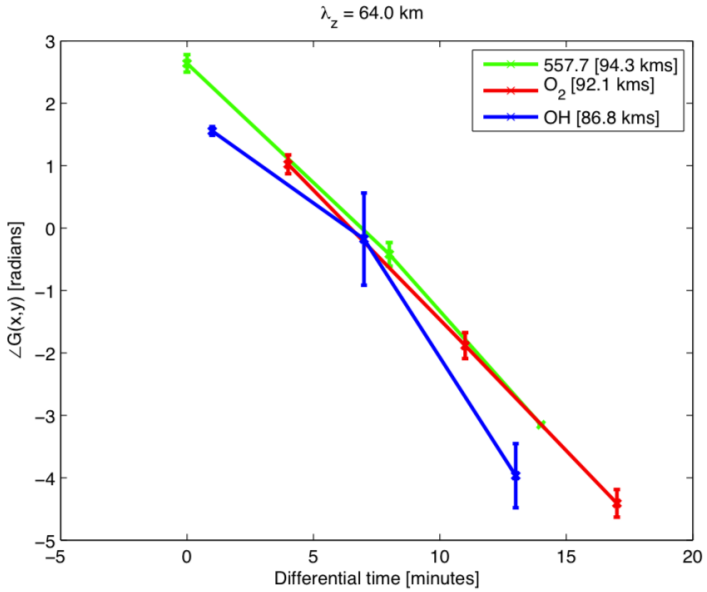

Figure 4.10 $\angle G(x, y)$ for all the three layers against time, in minutes, that is differenced to the time of the first observation. It can be inferred that along every emission layer there exists a constant slope implying a constant horizontal phase velocity of the wave. $\lambda_z = 64.0$ km.

Solving the following system of equations:

$$\begin{bmatrix} 2.637 \\ -0.4187 \\ -3.1511 \\ 1.5561 \\ -0.1757 \\ -3.9667 \\ 1.0226 \\ -1.8821 \\ -4.4099 \end{bmatrix} = \begin{bmatrix} 94.3 & 0 & 1 \\ 94.3 & 0.0056 & 1 \\ 94.3 & 0.0097 & 1 \\ 86.8 & 0.0007 & 1 \\ 86.8 & 0.0049 & 1 \\ 86.8 & 0.0090 & 1 \\ 92.1 & 0.0028 & 1 \\ 92.1 & 0.0076 & 1 \\ 92.1 & 0.0118 & 1 \end{bmatrix} \times \begin{bmatrix} k_z \\ \omega_t \\ \phi(x, y) \end{bmatrix}$$

yields $\lambda_z = 64.0$ km. Figure 4.10 plots $\angle G(x, y)$ for all the three layers against time, in minutes from the time of the first observation. It can be seen that along every emission layer there exists a constant slope, implying a constant horizontal phase velocity of the wave.

4.3.2 16 May 2010

On the night of 16 May 2010, AGWs perturbed the airglow emission layers with a horizontal wavelength much smaller than what was observed on the previous night. The projected airglow images acquired from NSO and Socorro at 07:54:16 UT are shown in Figure 4.11. The wavefronts propagate in the northwest direction similar to the previous night.

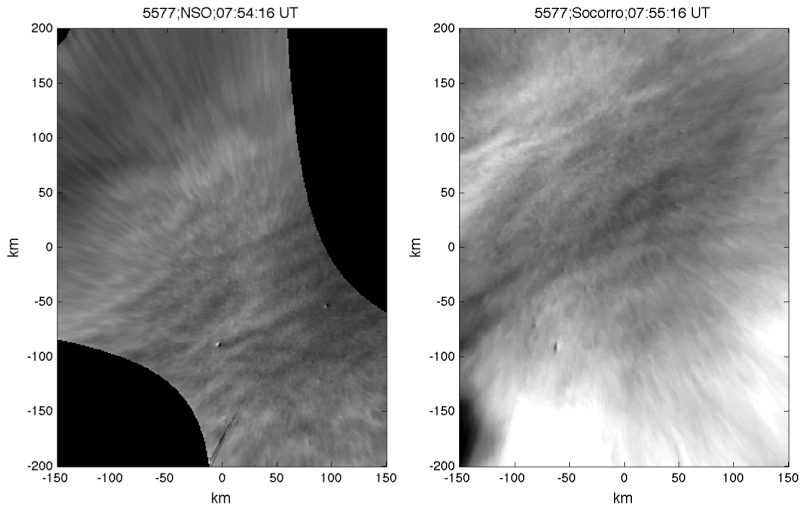

Figure 4.11 The projected airglow images acquired from NSO and Socorro at 07:54:16 UT on 16 May 2010.

The parameters of the Gabor filter, T and θ, are determined from an exhaustive search with the search space result presented in Figure 4.12.

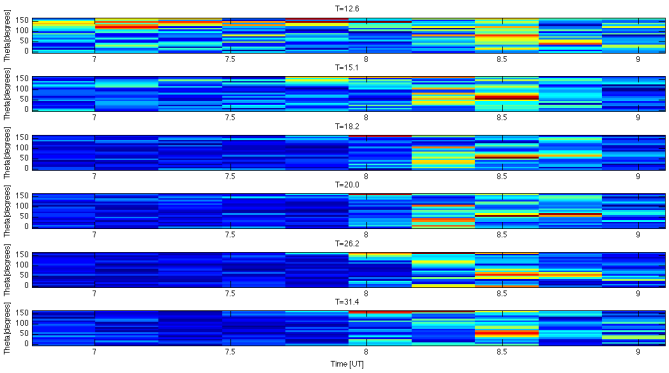

Figure 4.12 The parameters of the Gabor filter, T and θ, are determined from an exhaustive search with T ranging from 12.6 to 31.4 km and θ from 0° to 180°. $T = 20$ km and $\theta = 118°$.

Through manual examination of the orientation and λ_h of the wavefronts in the projected images, a rough estimate can be obtained for T and θ. This enables us to set a range to search within and eliminate instances that are physically inconsistent. The parameters are determined to be $T = 20$ km and $\theta = 118°$.

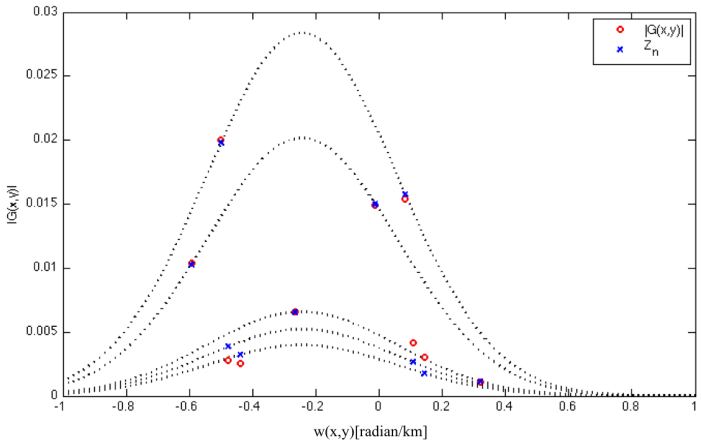

Figure 4.13 The five points chosen for the magnitude analysis are (10,-45), (17,-93), (-8,-67), (50,-44) and (-19,-2). For this set of points the model converges to the data, with $\lambda_z = 25.7$ km.

The five points chosen for the magnitude analysis are (10,-45), (17,-93), (-8,-67), (50,-44) and (-19,-2). For this set of points the model converges to the data, with $\lambda_z = 25.7$ km. The lack of fit in the data and model, as seen in Figure 4.13, can be attributed to degradation of the image resolution for points close to the edges. However, given the constraints, the best fit was achieved with the chosen set of points. This result is compared to the phase analysis with images at times listed in Table 4.2.

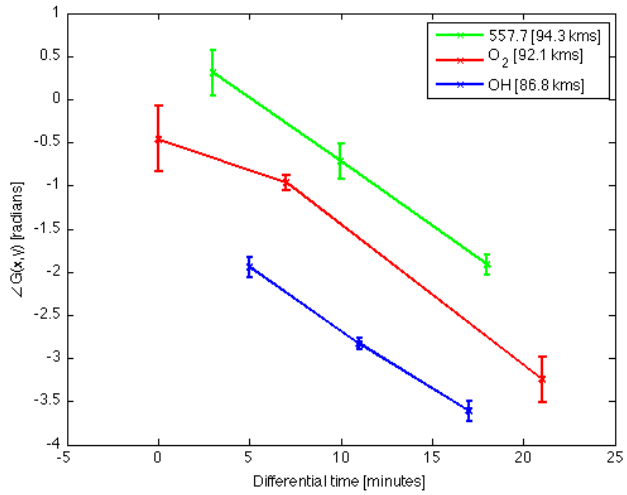

Figure 4.14 $\angle G(x, y)$ for all the three layers against time, in minutes, that is differenced to the time of the first observation. It can be inferred that along every emission layer there exists a constant slope implying a constant horizontal phase velocity of the wave. $\lambda_z = 25.7$ km.

Table 4.2 Timestamps of the images used for phase analysis, 16 May 2010

Emission	Height (km)	t_1 (UT)	t_2 (UT)	t_3 (UT)
Greenline	94.3	07:39:16	07:46:16	07:54:16
O_2	92.1	07:36:16	07:43:16	07:57:16
OH	86.8	07:41:16	07:47:16	07:53:16

The following system of equations is solved:

$$\begin{bmatrix} 0.3083 \\ -0.7183 \\ -1.9161 \\ -1.9437 \\ -2.8278 \\ -3.6076 \\ -0.4596 \\ -0.9599 \\ -3.2462 \end{bmatrix} = \begin{bmatrix} 94.3 & 0.0021 & 1 \\ 94.3 & 0.0069 & 1 \\ 94.3 & 0.0125 & 1 \\ 86.8 & 0.0035 & 1 \\ 86.8 & 0.0076 & 1 \\ 86.8 & 0.0118 & 1 \\ 92.1 & 0 & 1 \\ 92.1 & 0.0049 & 1 \\ 92.1 & 0.0146 & 1 \end{bmatrix} \times \begin{bmatrix} k_z \\ \omega_t \\ \phi(x,y) \end{bmatrix}.$$

The error bars in Figure 4.14 denote the upper and lower bound of the error in each value of $\angle G(x, y)$ which causes the discrepancies in vertical wavelength computed from the phase and magnitude of airglow perturbation model. λ_z is determined and is equal to 25.7 km.

4.3.3 2 September 2010

The wavefronts of the AGW observed by the two imagers on 2 September 2010 propagate towards the northeast through their fields of view. The change in the direction of propagation of the wavefronts could be attributed to the seasonality of the tropospheric winds that change direction. In Figure 4.15, the projected images acquired from the two sites at 05:13:02 UT are shown along with the five points used in the magnitude analysis.

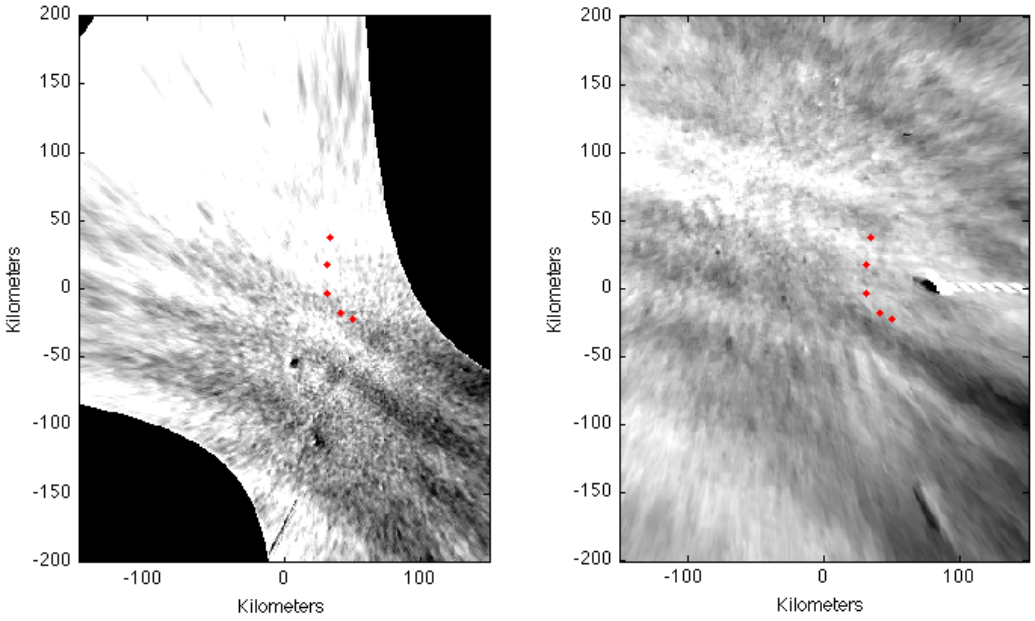

Figure 4.15 The projected airglow images acquired from NSO and Socorro at 05:13:02 UT on 2 September 2010. The five red points are used towards the magnitude analysis

These images are filtered using a Gabor filter with parameters $T = 36.5$ km and $\theta = 55.2°$. The magnitude of the Gabor filtered image from NSO is shown in Figure 4.16, where a single Gaussian like feature implies a filter well-matched to the spatial frequencies of observed AGW-induced airglow perturbation. The black crosses denote the five points - (31,-3), (41,-18), (34,38), (50,-22) and (31,18) - used towards the magnitude analysis. These points are determined by the minimizing the function described in Section 4.3.1. The model and the ten data points are plotted in Figure 4.17 and there is excellent match between the two with $\lambda_z = 41.8$ km.

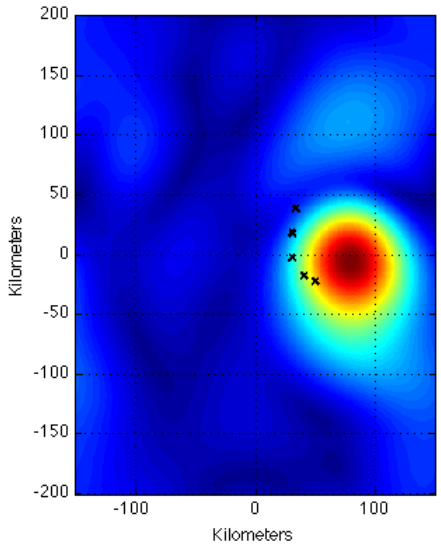

Figure 4.16 The parameters of the Gabor are determined, $T = 36.5$ km and $\theta = 55.2°$. The figure plots the magnitude of the filtered image. The black crosses denote the five points - (31,-3), (41,-18), (34,38), (50,-22) and (31,18) - used towards the magnitude analysis.

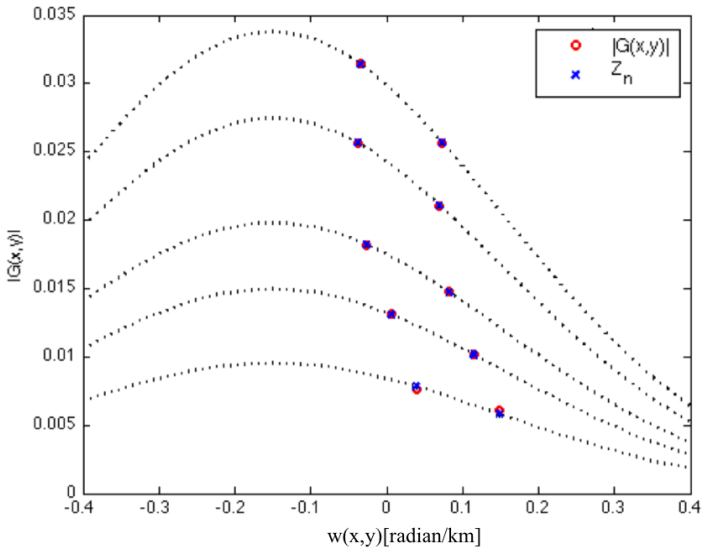

Figure 4.17 The model, Z_n, and the ten data points, $|G(x, y)|$, are plotted and there is excellent match between the two with $\lambda_z = 41.8$ km.

Table 4.3 lists the timestamps for the images used in the phase analysis. The phase is unwrapped and the following system is solved:

$$\begin{bmatrix} 1.3013 \\ 2.3733 \\ 3.0001 \\ 0.0655 \\ 0.8983 \\ 1.1660 \\ 0.6116 \\ 1.5821 \\ 2.2435 \end{bmatrix} = \begin{bmatrix} 94.3 & 0.0021 & 1 \\ 94.3 & 0.0069 & 1 \\ 94.3 & 0.0125 & 1 \\ 86.8 & 0.0007 & 1 \\ 86.8 & 0.0049 & 1 \\ 86.8 & 0.0090 & 1 \\ 92.1 & 0 & 1 \\ 92.1 & 0.0049 & 1 \\ 92.1 & 0.0104 & 1 \end{bmatrix} \times \begin{bmatrix} k_z \\ \omega_t \\ \phi(x,y) \end{bmatrix}$$

giving $\lambda_z = 41.5$ km. Figure 4.18 plots $\angle G(x,y)$ for the three emission layers used.

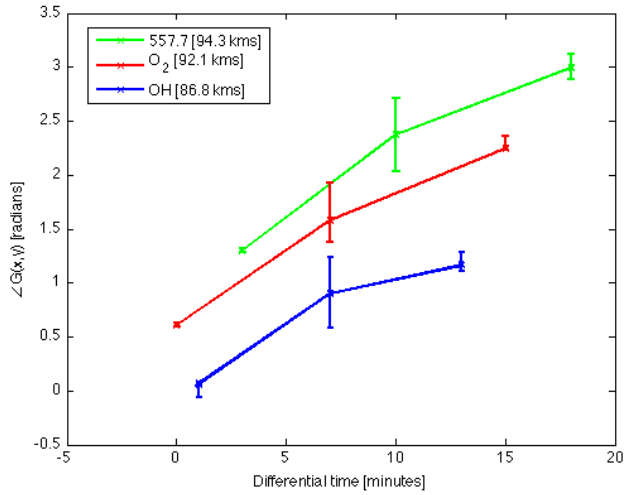

Figure 4.18 $\angle G(x,y)$ for all the three layers against time, in minutes, that is differenced to the time of the first observation at 5:03:02 UT on 2 September 2010. It can be inferred that along every emission layer there exists a constant slope implying a constant horizontal phase velocity of the wave. $\lambda_z = 41.5$ km.

Table 4.3 Timestamps of the images used for phase analysis, 2 September 2010

Emission	Height (km)	t_1 (UT)	t_2 (UT)	t_3 (UT)
Greenline	94.3	05:06:02	05:13:02	05:21:02
O_2	92.1	05:03:02	05:10:02	05:18:02
OH	86.8	05:04:02	05:10:02	05:16:02

4.4 Summary

The result of the parameter estimation techniques for three nights is summarized in Table 4.4. The estimates computed from the phase and magnitude analysis match to within a kilometer of each other, validating the model for an AGW-induced perturbed airglow emission layer as a quasi-monochromatic wave on these nights. It is shown that the vertical wavelength can be reliably estimated using observations from two ground-based imagers. These estimates can be further used to quantify the momentum and energy transported by AGWs to upper regions of the mesosphere.

Table 4.4 Summary of the results

Day of the year	λ_z(kms) from $\lvert G(x,y)\rvert$	λ_z(kms) from $\angle G(x,y)$
135	64.6	64.0
136	25.7	25.7
245	41.8	41.5

CHAPTER 5

CONCLUSIONS

This thesis studies the modulation of the airglow emission layers, between 80-100 km, by vertically propagating gravity waves that transport energy and momentum thereby altering the dynamics of the upper atmosphere. In order to quantify these effects in terms of the vertical energy flux or the vertical momentum flux, measurements of either ω_t or λ_z are needed. Using ground-based imagers, it is shown that λ_z can be estimated reliably. The vertical wavelength is estimated by applying a parameter estimation technique on the phase and magnitude of a model relating the perturbed airglow to the value of a pixel of a CCD on an imager observing it. The two estimates for λ_z from the phase and magnitude for a given night match to within a kilometer. It is also noted that the propagation direction of the wavefronts of the quasi-monochromatic AGWs shifts from northwest to northeast, suggesting that the structures are driven by tropospheric winds, whose direction varies seasonally. A di rect result of this is observed in the measurements made towards the end of the year when the wavefronts become increasingly parallel to the line joining the two imagers. This makes it hard to make a periodic observation of the wave. In this case, the line-of-sight vectors of both the imagers are integrating along the wavefront instead of across it and thus, there is no information of spatial periodicity of the wave in the measurements. This makes the data observed towards the end of the year largely unusable. The differences in estimates of λ_z computed from the

phase and magnitude might be reduced if the observations made were synchronous in time. As the waves propagate about a quarter to half a wavelength in 5 minutes, observations separated in time at this scale will be observing different wavefronts. Synchronicity is corrected for in the phase analysis by incorporating the $\omega_t t$ term, while with the magnitude analysis there is a handicap to choose images of the green-line that are synchronous. The issue of asynchronicity was addressed and in 2011, the data collected was temporally coincident. Results from three nights in 2010 are presented and the estimates of λ_z from both techniques on each night match to within a kilometer of each other and hence, the model is validated.

The modeling of AGWs as quasi-monochromatic waves is an important step towards understanding their overall morphology. These theoretical and modeling studies will contribute important quantitative information on gravity wave excitation, propagation, and dissipation mechanisms in the middle atmosphere. As AGWs propagate vertically, they exhibit significant coupling effects on different atmospheric regions. With knowledge of the vertical wavelength, the momentum and energy transported upwards from the troposphere can be quantified to understand AGW effects on large-scale wind and temperature fields. Gravity waves driven by the mean meridional circulation affect the transport of constituents such as ozone and ozone-destroying chemicals. Thus, climate change simulations can be made more accurate with precise quantitative knowledge of these transport mechanisms.

REFERENCES

Anderson, D. S., F. Kamalabadi, and G. R. Swenson (2009), Estimation of three-dimensional atmospheric wave parameters from ground-based spectroscopic airglow image data, *IEEE Transactions on Geoscience and Remote Sensing*, *47*(8), 2427–2435.

Austen, J. R., S. J. Franke, C. H. Liu, and K. C. Yeh (1986), Application of computerized tomography techniques to ionospheric research, in *International Beacon Satellite Symposium on Radio Beacon Contribution to the Study of Ionization and Dynamics of the Ionosphere and to Corrections to Geodesy and Technical Workshop*, vol. 1, edited by H. Minakoshi and K. Sinno, pp. 25–35, University of Oulu, Finland.

Austen, J. R., S. J. Franke, and C. H. Liu (1988), Ionospheric imaging using computerized tomography, *Radio Science*, *23*(3), 299–307.

Bates, D. R. (1978), Forbidden oxygen and nitrogen lines in the nightglow, *Planetary and Space Science*, *26*(10), 897–912.

Bates, D. R. (1981), The green light of the night sky, *Planetary and Space Science*, *29*(10), 1061–1067.

Bradfoot, A. L., and K. R. Kendall (1968), The airglow spectrum, 3100-10000 Å, *Journal of Geophysical Research*, *73*(1), 426–428.

Cogger, L. L., R. D. Elphinstone, and J. S. Murphree (1981), Temporal and latitudinal 5577 Å airglow variations, *Canadian Journal of Physics*, *59*(10), 1296–1307.

Dornbrack, A. (1998), Turbulent mixing by breaking gravity waves, *The Journal of Fluid Mechanicas*, *375*, 113–141.

Einaudi, F., and J. J. Finnigan (1981), The interaction between an internal gravity wave and the planetary boundary layer, *Quarterly Journal of the Royal Meteorological Society*, *107*(454), 807–832.

Frey, S., S. B. Mende, and H. U. Frey (2001), Satellite limb tomography applied to airglow of the 630 nm emission, *Journal of Geophysical Research*, *106*(A10), 21367–21380.

Fritts, D. C., and R. A. Vincent (1987), Mesospheric momentum flux studies at Adelaide, Australia: Observations and a gravity wave-tidal interaction model, *Journal of the Atmospheric Sciences*, *44*(3), 605–619.

Goldstein, S. (1931), On the stability of superposed streams of fluids of different densities, *Proceedings of the Royal Society A*, (132), 524–548.

Gossard, E. E., and W. H. Hooke (1975), *Waves in the Atmosphere*, Elsevier, New York.

Grebowsky, J. M., and A. C. Aikin (2002), *Meteors in the Earth's Atmosphere*, Cambridge University Press.

Hauf, T., U. Finke, J. Neisser, G. Bull, and J. G. Stangenberg (1996), A ground-based network for atmospheric pressure fluctuations, *Journal of Atmospheric and Oceanic Technology*, *13*(5), 1001–1023.

Hecht, J. H., R. L. Walterscheid, and R. A. Vincent (2001a), Airglow observations of dynamical (wind shear-induced) instabilities over Adelaide, Australia, associated with atmospheric gravity waves, *Journal of Geophysical Research*, *106*(D22), 28189–28197.

Hecht, J. H., R. L. Walterscheid, M. P. Hickey, and S. J. Franke (2001b), Climatology and modeling of quasi-monochromatic atmospheric gravity waves observed over Urbana, Illinois, *Journal of Geophysical Research*, *106*(D6), 5181–5195.

Hines, C. O. (1965), Dynamical heating of the upper atmosphere, *Journal of Geophysical Research*, *70*(1), 177–183.

Kane, T. J., C. S. Gardner, Q. Zhou, J. D. Mathews, and C. A. Tepley (1993), Lidar, radar and airglow observations of a prominent sporadic Na/sporadic E layer event at Arecibo during AIDA-89, *Journal of Atmospheric and Terrestrial Physics*, *55*(3), 499–511.

Kopp, E. (1997), On the abundance of metal ions in the lower ionosphere, *Journal of Geophysical Research*, *102*(A5), 9667–9674.

Liu, A. Z., and G. R. Swenson (2003), A modeling study of O_2 and OH airglow perturbations induced by atmospheric gravity waves, *Journal of Geophysical Research*, *108*(D4), 4151.

McDade, I. C., D. P. Murtagh, R. G. H. Greer, P. H. G. Dickinson, G. Witt, J. Stegman, E. J. Llewellyn, L. Thomas, and D. B. Jenkins (1986), ETON 2: Quenching parameters for the proposed precursors of $O_2(b^1\sum_g{}^+)$ and O(^{1}S) in the terrestrial nightglow, *Planetary and Space Science*, *34*(9), 789–800.

Meinel, A. B. (1950), OH emission bands in the spectrum of the night sky, *Astrophysical Journal*, *111*, 555.

Nappo, C. J. (2002), *An Introduction to Atmospheric Gravity Waves*, chap. 1: Fundamentals, pp. 1 – 24, Academic Press, San Diego.

Nygren, T., M. J. Taylor, M. S. Lehtinen, and M. Markkanen (1998), Application of tomographic inversion in studying airglow in the mesopause region, *Annales Geophysicae*, *16*(10), 1180–1189.

Nygren, T., M. J. Taylor, G. R. Swenson, and M. S. Lehtinen (2000), Observing gravity wave activity in the mesopause region by means of airglow tomography, *Advances in Space Research*, *26*(6), 903–906.

Pearce, F. (2006), Introduction: Climate change. Available at http://www.newscientist.com/article/dn9903-instant-expert-climate-change.html.

Peterson, A. W. (1979), Airglow events visible to the naked eye, *Applied Optics*, *18*(20), 3390–3393.

Peterson, A. W., and G. W. Adams (1983), OH airglow phenomena during the 5–6 July 1982 total lunar eclipse, *Applied Optics*, *22*(17), 2682–2685.

Peterson, A. W., and L. M. Kieffaber (1973), Infrared photography of OH airglow structures, *Nature*, *242*(5396), 321–322.

Reisin, E. R., and J. Scheer (1996), Characteristics of atmospheric waves in the tidal period range derived from zenith observations of O_2 (0-1) atmospheric and OH (6-2) airglow at lower midlatitudes, *Journal of Geophysical Research*, *101*(D16), 21223–21232.

Sharp, W. E. (1986), Sources of the emission features between 2000 and 8000 Å in the thermosphere, *Canadian Journal of Physics*, *64*(12), 1594–1607.

Solomon, S. C., and R. R. Garcia (1987), Current understanding of mesospheric transport processes, *Philosophical Transactions - Royal Society of London, A*, *323*(1575), 655–666.

Solomon, S. C., P. B. Hays, and V. J. Abreu (1984), Tomographic inversion of satellite photometry, *Applied Optics*, *23*(19), 3409–3414.

Swenson, G. R., J. Tang, F. Kamalabadi, and S. J. Franke (2005), Methods of deducing intrinsic measurements of high frequency atmospheric gravity waves (AGWs), in *SPIE, Remote Sensing of Clouds and Atmosphere X*, vol. 5979, edited by K. Schaefer, A. Comeron, J. R. Slusser, R. H. Picard, M. R. Carleer, and N. Sifakis, pp. 261–269.

Taylor, G. I. (1931), Effect of variation in density on the stability of superposed streams of fluid, *Proceedings of the Royal Society of London. Series A, Containing Papers of a Mathematical and Physical Character*, *132*(820), 499–523.

Taylor, M. J., Y. Y. Gu, X. Tao, C. S. Gardner, and M. B. Bishop (1995), An investigation of intrinsic gravity wave signatures using coordinated lidar and nightglow image measurements, *Geophysical Research Letters*, *22*(20), 2853–2856.

Taylor, M. J., J. Pendleton, W. R., S. Clark, H. Takahashi, D. Gobbi, and R. A. Goldberg (1997), Image measurements of short-period gravity waves at equatorial latitudes, *Journal of Geophysical Research*, *102*(D22), 26283–26299.

Texier, H. L., S. C. Solomon, and R. R. Garcia (1987), Seasonal variability of the OH Meinel bands, *Planetary and Space Science*, *35*(8), 977–989.

Torr, M. R., D. G. Torr, and R. R. Laher (1985), The O_2 atmospheric 0-0 band and related emissions at night from Spacelab 1, *Journal of Geophysical Research*, *90*(A9), 8525–8538.

Vargas, F., G. R. Swenson, A. Z. Liu, and D. Gobbi (2007), $O(^1S)$, OH, and O_2(b) airglow layer perturbations due to AGWs and their implied effects on the atmosphere, *Journal of Geophysical Research - Atmospheres*, *112*(D14), D14102.

Viereck, R. A., and C. S. Deehr (1989), On the interaction between gravity waves and the OH Meinel (6-2) and the O_2 atmospheric (0-1) bands in the polar night airglow, *Journal of Geophysical Research*, *94*(A5), 5397–5404.

Walterscheid, R. L., J. H. Hecht, R. A. Vincent, I. M. Reid, J. Woithe, and M. P. Hickey (1999), Analysis and interpretation of airglow and radar observations of quasi-monochromatic gravity waves in the upper mesosphere and lower thermosphere over Adelaide, Australia (35° S, 138° E), *Journal of Atmospheric and Solar-Terrestrial Physics*, *61*(6), 461–478.

Zamora, R. L. (1983), Studies in nocturnal stable layers at BAO, tech. rep., NOAA/ERL, Boulder, CO.

Zhang, S. P., R. N. Peterson, R. H. Wiens, and G. G. Shepherd (1993), Gravity waves from O_2 nightglow during the AIDA '89 campaign I: Emission rate/temperature observations, *Journal of Atmospheric and Terrestrial Physics*, *55*(3), 355–375.